ATLAS NOTE

ATLAS-CONF-2012-098

August 30, 2012

Observation of an Excess of Events in the Search for the Standard Model Higgs Boson in the $H \rightarrow WW^{(*)} \rightarrow \ell\nu\ell\nu$ Channel with the ATLAS Detector

The ATLAS Collaboration

Abstract

A Standard Model Higgs boson search in the $H \rightarrow WW^{(*)} \rightarrow e\nu\mu\nu$ decay mode has been performed using proton-proton collision data corresponding to an integrated luminosity of 5.8 fb^{-1} at a centre-of-mass energy of 8 TeV collected during 2012 with the ATLAS detector at the Large Hadron Collider. The search focuses on the mass region around 125 GeV, not previously excluded, where an excess of events over the expected background is observed corresponding to a local p_0-value of 6×10^{-4} or 3.2 standard deviations. In a combined analysis of the 2012 data with the 4.7 fb^{-1} of data acquired at $\sqrt{s}$ = 7 TeV in 2011, the observed excess in the $H \rightarrow WW^{(*)} \rightarrow \ell\nu\ell\nu$ channel corresponds to a minimum local p_0 of 3×10^{-3} or 2.8 standard deviations.

This note has been modified from the original version dated 17 July to correct and improve the presentation. The results of the analysis are unchanged. The systematic uncertainties given in Table 4 were for the expected signal and backgrounds without upper and lower m_T thresholds, and have been changed to the uncertainties with the m_T thresholds applied. The systematic uncertainty on the muon fake factor was incorrectly stated as 60%; it is 40% and has been corrected. The single top and $Z \rightarrow 4\ell$ cross sections have been corrected in Table 1. The uncertainty on the normalisation factor for the top background in the $H + 2$-jet analysis now includes the statistical uncertainty from the number of events in the control region. The best-fit μ value is quoted at m_H = 126 GeV, not 125 GeV, for consistency with the published results. Finally, there have been some small modifications to clarify the text.

1 Introduction

The Standard Model (SM) of particle physics [1–3] has been tested by many experiments over the last four decades and has been shown to successfully describe high energy phenomena. However, the mechanism that breaks electroweak symmetry in the SM still remains to be confirmed experimentally. This mechanism [4–6], which gives mass to all massive elementary particles, predicts the existence of a scalar particle, the Higgs boson. It is the only elementary particle in the SM that has not yet been observed and the search for the Higgs boson is a centrepiece of the LHC physics programme.

Indirect limits on the Higgs boson mass of $m_H < 158$ GeV at 95% confidence level (CL) have been set using global fits to precision electroweak results [7]. Direct searches at LEP and the Tevatron have excluded at 95% CL a SM Higgs boson with a mass below 114.4 GeV [8] and in the regions 147 GeV $< m_H <$ 180 GeV and 100 GeV $< m_H <$ 103 GeV [9], respectively.

The results of searches in various channels using $\sqrt{s} = 7$ TeV data corresponding to an integrated luminosity of approximately 5 fb^{-1} have been reported recently by the ATLAS Collaboration, excluding the mass ranges 112.9 GeV–115.5 GeV, 131 GeV–238 GeV, and 251 GeV–466 GeV [10]; and by the CMS Collaboration, excluding the mass range from 127 GeV to 600 GeV [11]. Due to the narrow region remaining in m_H after the exclusions made from the 2011 data, the hypothesis of $m_H = 125$ GeV is used to characterise the signal for many aspects of the search presented here.

The $H \rightarrow WW^{(*)} \rightarrow \ell\nu\ell\nu$ channel (with $\ell = e, \mu$) is particularly sensitive in the mass range $120 < m_H < 200$ GeV. This channel can play an important role in the determination of the coupling of the Higgs boson to W bosons. The branching ratio to WW falls off with decreasing m_H below $m_H = 2m_W$ but is still just over 20% at $m_H = 125$ GeV [12], and the dilepton final state allows the selection of events with a favourable signal-to-background ratio. The leading backgrounds are continuum $WW \rightarrow \ell\nu\ell\nu$ production and $t\bar{t}$ events in which both W bosons decay to $\ell\nu$. Additional sources of background include Drell-Yan ($pp \rightarrow Z/\gamma^* \rightarrow \ell\ell$), W+jets, single top, $W(Z/\gamma^{(*)})$, and ZZ events.

The previous $H \rightarrow WW^{(*)} \rightarrow \ell\nu\ell\nu$ search results reported by the ATLAS collaboration used the full 2011 dataset, corresponding to 4.7 fb^{-1} of proton-proton (pp) collisions at $\sqrt{s} = 7$ TeV, and excluded a SM Higgs boson in the mass range 133 GeV $< m_H <$ 261 GeV at 95% CL [13]. A similar search has been performed by the CMS Collaboration [14]. The analysis described here uses a dataset collected between the beginning of April to the middle of June 2012, which after requiring that all detector components are fully functional, corresponds to 5.8 fb^{-1} of pp collision data at a centre-of-mass of 8 TeV. The production cross section of a Higgs boson with $m_H = 125$ GeV increases by about 30% with the increase of the centre-of-mass energy of the Large Hadron Collider from 7 TeV to 8 TeV. The analysis methodology reported in Ref. [13] is mostly unchanged, but some selection criteria have been modified to reduce background contributions while coping with the higher instantaneous luminosity of the LHC in 2012. In particular, the data are affected by the occurrence of multiple pp collisions per bunch crossing, referred to as "pile-up". In the 2011 data the average number of interactions per bunch crossing was around 10. In 2012, the average has increased to around 20. This results in significantly larger Drell-Yan background to the same-flavour final states, due to an increased rate of fake missing transverse energy. Since the $e\mu$ final state provides the large majority of the sensitivity of the search, only this final state has been used in the analysis reported here. Finally, more stringent isolation criteria are applied, to further reduce the W+jets background.

Motivated by the 2011 combined Higgs searches [10], the analysis procedure was modified to blind the kinematic region where a signal might be expected. Events passing the kinematic selection designed to isolate a signal from a SM Higgs boson with a mass between 110 and 140 GeV were excluded during the development of the 2012 analysis. The signal region data were unblinded once the agreement between data and the background model in the control regions corresponding to the

dominant backgrounds was judged to be reasonable.

In the last part of this document, the results obtained at $\sqrt{s}$ = 8 TeV with 5.8 fb^{-1} of data are combined with the published $H \to WW^{(*)} \to \ell\nu\ell\nu$ results from the 2011 dataset.

2 Data and simulated samples

The data used for this analysis were collected in 2012 using the ATLAS detector, a multi-purpose particle physics experiment with a forward-backward symmetric cylindrical geometry and near 4π coverage in solid angle [15]. ATLAS consists of an inner tracking detector surrounded by a thin superconducting solenoid, electromagnetic and hadronic calorimeters, and an external muon spectrometer incorporating large superconducting air-core toroid magnets. The combination of these systems provides charged particle measurements together with efficient and precise lepton measurements over the pseudorapidity[1] range $|\eta| < 2.5$. Jets are reconstructed over the full coverage of the calorimeters, $|\eta| < 4.9$; this calorimeter coverage also provides a measurement of the missing transverse momentum $E_{\mathrm{T}}^{\mathrm{miss}}$.

The data used for this analysis were collected using inclusive single-muon and single-electron triggers. The two main triggers require the transverse momentum of the lepton with respect to the beam line, p_{T}, to exceed 24 GeV and that the lepton be isolated: the scalar sum of the p_{T} of charged particles within $\Delta R = \sqrt{\Delta\phi^2 + \Delta\eta^2} = 0.2$ of the lepton direction is required to be less than 0.12 and 0.10 times the lepton p_{T} for the muon and electron, respectively. Because of the detector geometry, the acceptance of the muon trigger is limited to $|\eta| < 2.4$. The trigger efficiencies are measured as a function of p_{T}, η, and data-taking period using Z events. The efficiencies are approximately 90% for electrons, and 90% (70%) for muons in the endcap (barrel).

In this analysis, the signal contributions considered include the dominant gluon fusion production process ($gg \to H$, denoted as ggF), the vector-boson fusion production process ($qq' \to qq'H$, denoted as VBF) and the Higgs-strahlung process ($qq' \to WH, ZH$, denoted as WH/ZH). The $t\bar{t}H$ production mechanism is negligible due to its smaller cross section. For the decay of the Higgs boson, only the $H \to WW^{(*)} \to e\nu\mu\nu$ mode is considered, including the small contributions from leptonic τ decays. The branching fraction for this decay as a function of m_H is calculated using the Prophecy4f [30, 31] program, with HDECAY also used in calculating the total width [32].

The signal cross section is computed to next-to-next-to-leading order (NNLO) [33–38] in QCD for the ggF process using the MSTW2008 PDF set [39]. Next-to-leading order (NLO) electroweak (EW) corrections are also applied [40, 41], as well as QCD soft-gluon resummations up to next-to-next-to-leading log (NNLL) [42]. These calculations are detailed in Refs. [43, 44], and assume factorisation between the QCD and EW corrections.

Approximate NNLO QCD corrections [45] and full NLO QCD and EW corrections [46–48] and are used to calculate the cross sections for VBF signal production. The cross sections of the associated WH/ZH production processes are calculated up to NNLO QCD corrections [49, 50] and NLO EW corrections [51].

The Monte Carlo (MC) generators used to model signal and background processes are listed in Table 1. For most processes, separate programs are used to generate the hard scattering process and to model the parton showering, hadronisation, and the underlying event. PYTHIA [28] or PYTHIA8

---

[1]ATLAS uses a right-handed coordinate system with its origin at the nominal interaction point (IP) in the centre of the detector, and the z-axis along the beam line. The x-axis points from the IP to the centre of the LHC ring, and the y-axis points upwards. Cylindrical coordinates (r, ϕ) are used in the transverse plane, ϕ being the azimuthal angle around the beam line. The pseudorapidity is defined in terms of the polar angle θ as $\eta = -\ln\tan(\theta/2)$.

Table 1: MC generators used to model the signal and background processes, and the corresponding cross sections at $\sqrt{s} = 8$ TeV (given $m_H = 125$ GeV in the case of the signal processes). The ggF Higgs boson p_T spectrum in POWHEG [12] is tuned to agree with the prediction from HqT [16]. Finite heavy quark mass effects in the gluon-gluon production are also included [17]. The relevant single-top production channels (s-channel and Wt) are included. The number quoted for the inclusive Z/γ^* process (also referred to in the text as the Drell-Yan process) is for generated dilepton invariant masses greater than 10 GeV. Kinematic criteria are also applied in the generation of $W(\to \ell\nu)\gamma$ events (the photon must have $p_T > 8$ GeV and be separated from the charged lepton by $\Delta R = \sqrt{(\Delta\eta^2) + (\Delta\phi^2)} > 0.25$) and $W(\to \ell\nu)\gamma^*(\to \ell'\ell')$ events (at least two leptons have p_T larger than 5 GeV and $|\eta| < 3$ for the ee and $\mu\mu$ case, and $|\eta| < 5$ for the $\tau\tau$ case). The $Z^{(*)}Z^{(*)} \to 4\ell$ samples are generated with an invariant mass cut of $m_{\ell\ell} > 4$ GeV. For the $WZ^{(*)}$ and $W\gamma^*$ processes, MAD-GRAPH includes the interference between the $Z^{(*)}$ and the γ^*, and the boundary between the samples is at $m_{\ell\ell} = 7$ GeV. For the $W\gamma^*$ a lower invariant mass cut of $m_{\ell\ell} > 2m_e$ is applied. Leptonic decays of W/Z bosons are always assumed, and the quoted cross sections include the branching ratios and are summed over lepton flavours. The exception is top quark production; for which inclusive cross sections are quoted.

Process	Generator	m_H (GeV)	$\sigma \cdot$ Br (pb)
ggF	POWHEG [18]+PYTHIA8 [19]	125	0.441
VBF	POWHEG [20]+PYTHIA8	125	$35 \cdot 10^{-3}$
WH/ZH	PYTHIA8	125	$25 \cdot 10^{-3}$
$q\bar{q}/g \to WW$	MC@NLO [21]+HERWIG [22]		5.68
$gg \to WW$	GG2WW [23]+HERWIG		0.16
$t\bar{t}$	MC@NLO+HERWIG		238
tW/tb	MC@NLO+HERWIG		28
tqb	AcerMC [24]+PYTHIA		88
inclusive W	ALPGEN [25]+HERWIG		$37 \cdot 10^3$
inclusive Z/γ^*	ALPGEN+HERWIG		$16 \cdot 10^3$
$Z^{(*)}Z^{(*)} \to 4l$	POWHEG+PYTHIA8		0.73
$WZ^{(*)}$	MADGRAPH [26, 27]+PYTHIA [28]		1.54
$W\gamma^*$	MADGRAPH [29]+PYTHIA		9.26
$W\gamma$	ALPGEN+HERWIG		369

[19] are used for these latter three steps for the signal and some of the background processes. When HERWIG [22] is used for the hadronisation and parton showering the underlying event is modelled using JIMMY [52]. The MLM matching scheme [53] is used for the description of the W+jets, Z/γ^*+jets and $W\gamma$ processes. The cross sections for the $W\gamma$ and $W\gamma^*/WZ^{(*)}$ processes are normalised to the MCFM [54] NLO predictions. These normalisation factors (K-factors) are calculated to be 1.15 for $W\gamma$, 1.3 for $W\gamma^*$ ($m_{\ell\ell} < 7$ GeV) and 1.51 for $WZ^{(*)}$ ($m_{\ell\ell} > 7$ GeV).

The CT10 parton distribution function (PDF) set [55] is used for the POWHEG and MC@NLO samples, and CTEQ6L1 [56] is used for the ALPGEN, MadGraph, and PYTHIA8 samples. Acceptances and efficiencies are obtained from a full simulation [57] of the ATLAS detector using GEANT4 [58]. The simulation incorporates a model of the pile-up conditions in the 2012 data, including both the effects of multiple pp collisions in the same bunch crossing ("in-time" pile-up) and in nearby bunch crossings ("out-of-time" pile-up).

3

3 Event selection

Events are required to have a primary vertex consistent with the beam spot position, with at least three associated tracks with $p_T > 400$ MeV. Data quality criteria are applied to events in order to suppress non-collision backgrounds such as cosmic-ray muons, beam-related backgrounds, or noise in the calorimeters.

$H \rightarrow WW^{(*)} \rightarrow \ell\nu\ell\nu$ candidates (with $\ell = e,\, \mu$) are pre-selected by requiring exactly two oppositely charged leptons of different flavours, with p_T thresholds of 25 GeV and 15 GeV for the leading and sub-leading lepton, respectively. Events are classified into two exclusive lepton channels depending on the flavour of the leading lepton: in the following, $e\mu$ (μe) will refer to events with a leading electron (muon). The dilepton invariant mass is required to be greater than 10 GeV. For muons, the range $|\eta| < 2.5$ is used; for electrons, the range $|\eta| < 2.47$ is used, with the region $1.37 < |\eta| < 1.52$, corresponding to the boundary between barrel and end-cap calorimeters, excluded.

Electron candidates are selected by applying a set of tight identification criteria using a combination of tracking and calorimetric information. The fine lateral and longitudinal segmentation of the calorimeter and transition radiation capability of the ATLAS detector have allowed the previous levels of electron performance [59] to be retained in the increased pile-up environment of the 2012 data taking. Muon candidates are identified by matching tracks reconstructed in the inner detector and in the muon spectrometer [60]. Requirements on the number of hits in all three components of the inner detector (pixels, SCT, and TRT) provide background rejection, particularly against pion/kaon decays-in-flight.

At least one of the selected leptons is required to match a triggering object. Leptons from heavy-flavour decays and jets satisfying the lepton identification criteria are suppressed by requiring the leptons to be isolated: the scalar sum of the p_T of charged particles and of the calorimeter energy deposits within $\Delta R = \sqrt{\Delta\phi^2 + \Delta\eta^2} = 0.3$ of the lepton direction (excluding the lepton itself) are each required to be less than $0.12 - 0.20$ times the lepton p_T. The exact value differs between the track- and calorimeter-based criteria, between electrons and muons, and depend on the lepton p_T.

Drell-Yan and QCD multijet events are suppressed by requiring large E_T^{miss} [61]. The E_T^{miss} is the magnitude of $\mathbf{E}_T^{\text{miss}}$, the opposite of the vector sum of the transverse momenta of the reconstructed objects, including muons, electrons, photons, jets, and clusters of calorimeter cells not associated with these objects. The quantity $E_{T,\text{rel}}^{\text{miss}}$ used in this analysis is defined as: $E_{T,\text{rel}}^{\text{miss}} = E_T^{\text{miss}} \sin \Delta\phi_{\text{min}}$, with $\Delta\phi_{\text{min}} \equiv \min(\Delta\phi, \frac{\pi}{2})$. Here, $\Delta\phi$ is the minimum azimuthal angle between $\mathbf{E}_T^{\text{miss}}$ and the leading lepton, the sub-leading lepton or any jet with $p_T > 25$ GeV.

Compared to E_T^{miss}, the use of $E_{T,\text{rel}}^{\text{miss}}$ increases the rejection of events with significant mismeasurement of a jet or a lepton, since in such events the direction in ϕ of the $\mathbf{E}_T^{\text{miss}}$ is correlated with the direction of the mismeasured object. Figure 1 shows the distribution of $E_{T,\text{rel}}^{\text{miss}}$ in dilepton events passing all of the selection above, up to but not including the $E_{T,\text{rel}}^{\text{miss}}$ threshold. The threshold applied in this analysis is 25 GeV. Any multijet background present at this stage is included in the W+jets background estimate. After the lepton isolation and $E_{T,\text{rel}}^{\text{miss}}$ requirements, the multijet background is negligible and the Drell-Yan background is much reduced. The Drell-Yan contribution becomes negligible after the topological selections, described later in this section, are applied.

Figure 1 shows the multiplicity distribution of jets reconstructed using the anti-k_t algorithm [62], with distance parameter $R = 0.4$, for all events satisfying the pre-selection criteria described above including the $E_{T,\text{rel}}^{\text{miss}}$ requirement. Only jets with $p_T > 25$ GeV and $|\eta| < 4.5$ are considered. The jet p_T threshold is increased to 30 GeV in the forward region $2.5 < |\eta| < 4.5$ to reduce the contribution from jets produced by pile-up. In order to reject jets that are produced in the central part of the detector by
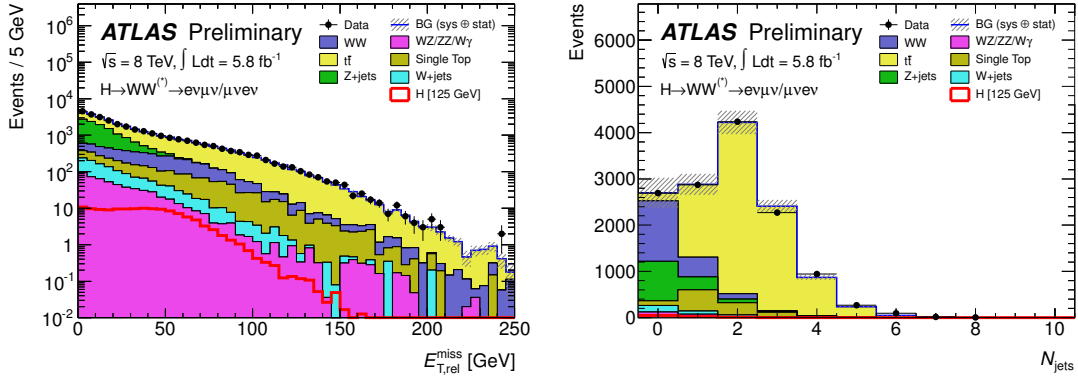
4

Figure 1: $E_{\mathrm{T,rel}}^{\mathrm{miss}}$ (left) and multiplicity of jets (right) for events satisfying the pre-selection criteria described in the text. (No $E_{\mathrm{T,rel}}^{\mathrm{miss}}$ requirement is applied in the $E_{\mathrm{T,rel}}^{\mathrm{miss}}$ distribution.) The jet selection applied is $p_T^{jet} > 25$ GeV for $|\eta^{jet}| < 2.5$ and $p_T^{jet} > 30$ GeV for $2.5 < |\eta^{jet}| < 4.5$. The lepton channels are combined. The hashed area indicates the total uncertainty on the background prediction. The WW and top backgrounds are scaled to use the normalisation derived from the corresponding control regions described in the text. The expected signal for a SM Higgs boson with $m_H = 125$ GeV is superimposed.

pile-up interactions, a selection criterion is applied to each jet with $|\eta| < 2.5$ on a quantity called the jet vertex fraction (JVF). The JVF is defined, using the charged tracks associated with a given jet, to be the p_T sum of the tracks originating from the primary vertex divided by the p_T sum of all of the tracks. Jets are required to have JVF > 0.5. This selection was found to be robust against pile-up, based on studies of the dependence of the jet multiplicity on the number of reconstructed vertices in the 2012 Z+jet data. Figure 2 shows the ratio of $Z \rightarrow \mu\mu$ + 1-jet events to all $Z \rightarrow \mu\mu$ events as a function of the number of reconstructed primary vertices. The events are selected by applying the pre-selection criteria (excluding the $E_{\mathrm{T,rel}}^{\mathrm{miss}}$ requirement) with two muons and an additional requirement on the invariant mass ($|m_{\mu\mu} - m_Z| < 15$ GeV) in order to select Z events. No dependence is seen with the jet selection described above.

The background rate and composition depend significantly on the jet multiplicity, as does the signal topology. Without accompanying jets, the signal originates almost entirely from the ggF process and the background is dominated by WW and Drell-Yan events. In contrast, when produced in association with two or more jets, the signal contains a much larger contribution from the VBF process and the background is dominated by $t\bar{t}$ production. To maximise the sensitivity, further selection criteria that depend on the jet multiplicity are applied to the pre-selected sample. The data are subdivided into $H + 0$-jet, $H + 1$-jet and $H + 2$-jet channels according to the jet counting defined above (with the $H + 2$-jet channel also including higher jet multiplicities at this stage). The different requirements for these channels are described in more detail below.

Due to spin correlations in the $WW^{(*)}$ system arising from the spin-0 nature of the SM Higgs boson and the V-A structure of the W boson decay, the charged leptons tend to emerge from the interaction point in the same direction. This kinematic feature is exploited for all jet multiplicities by requiring that the azimuthal angular difference between the leptons, $\Delta\phi_{\ell\ell}$, be less than 1.8 radians, and that the dilepton invariant mass, $m_{\ell\ell}$, be less than 50 GeV for the $H + 0$-jet and $H + 1$-jet channels. For the $H + 2$-jet channel, the $m_{\ell\ell}$ upper bound is increased to 80 GeV. The $m_{\ell\ell}$ distribution is somewhat harder
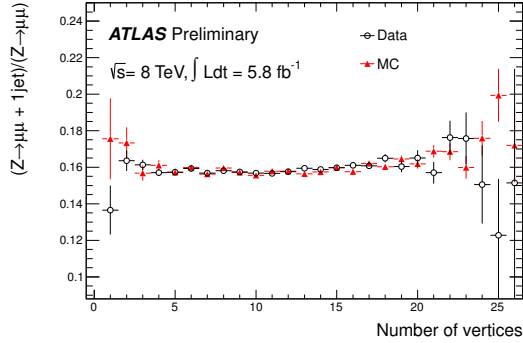
Figure 2: Ratio of $Z \to \mu\mu$ + 1-jet events to all $Z \to \mu\mu$ candidates as a function of the number of reconstructed primary vertices in the event. The selected events must pass the pre-selection criteria, excluding the $E_{\mathrm{T,rel}}^{\mathrm{miss}}$ requirement, with the additional selection of $|m_{\mu\mu} - m_Z| < 15$ GeV. Only statistical uncertainties are included.

for the H + 2-jet topology since the Higgs boson is more strongly boosted, reducing the alignment of the Ws and decorrelating the lepton directions.

In the H + 0-jet channel, the magnitude $p_{\mathrm{T}}^{\ell\ell}$ of the transverse momentum of the dilepton system, $\mathbf{p}_{\mathrm{T}}^{\ell\ell} = \mathbf{p}_{\mathrm{T}}^{\ell 1} + \mathbf{p}_{\mathrm{T}}^{\ell 2}$, is required to be greater than 30 GeV. This improves the rejection of the Drell-Yan background.

In the H + 1-jet channel, backgrounds from top quark decays are suppressed by rejecting events containing a jet identified as being consistent with originating from the decay of a b or c quark (b-tagged jet), using a b-tagging algorithm based on a neural network that exploits the topology of weak decays of b- and c-hadrons [63]. The algorithm is tuned to achieve an 85% b-jet identification efficiency in $t\bar{t}$ events while yielding a light-jet tagging rate of approximately 11% [64]. The total transverse momentum, $p_{\mathrm{T}}^{\mathrm{tot}}$, defined as the magnitude of the vector sum $\mathbf{p}_{\mathrm{T}}^{\mathrm{tot}} = \mathbf{p}_{\mathrm{T}}^{\ell 1} + \mathbf{p}_{\mathrm{T}}^{\ell 2} + \mathbf{p}_{\mathrm{T}}^{\mathrm{j}} + \mathbf{E}_{\mathrm{T}}^{\mathrm{miss}}$, is required to be smaller than 30 GeV to suppress top background events that have additional jets with p_{T} below threshold. The $\tau\tau$ invariant mass, $m_{\tau\tau}$, is computed under the assumption that the reconstructed leptons are τ lepton decay products, that the neutrinos produced in the τ decays are collinear with the leptons [65], and that they are the only source of $E_{\mathrm{T}}^{\mathrm{miss}}$. Events with $|m_{\tau\tau} - m_Z| < 25$ GeV are rejected if the energy fractions carried by the putative visible decay products are positive (the collinear approximation does not always yield physical solutions).

The H + 2-jet selection follows the H + 1-jet selection described above (with the $p_{\mathrm{T}}^{\mathrm{tot}}$ definition modified to include all selected jets). In addition, several additional jet-related criteria are applied to the two highest-p_{T} jets in the event, referred to as the "tag" jets. The tag jets must be separated in rapidity by a distance $|\Delta y_{\mathrm{jj}}|$ of at least 3.8. Events with an additional jet with $p_{\mathrm{T}} > 20$ GeV in between the tag jets ($y_{j1} < y < y_{j2}$) are vetoed. Finally, the invariant mass of the two tag jets, m_{jj}, must be at least 500 GeV.

A transverse mass variable, m_{T} [66], is used in this analysis to test for the presence of a signal for all jet multiplicities. This variable is defined as:

$$m_{\mathrm{T}} = \sqrt{(E_{\mathrm{T}}^{\ell\ell} + E_{\mathrm{T}}^{\mathrm{miss}})^2 - |\mathbf{p}_{\mathrm{T}}^{\ell\ell} + \mathbf{E}_{\mathrm{T}}^{\mathrm{miss}}|^2},$$

where $E_{\mathrm{T}}^{\ell\ell} = \sqrt{|\mathbf{p}_{\mathrm{T}}^{\ell\ell}|^2 + m_{\ell\ell}^2}$. The statistical analysis of the candidate data uses a fit to the m_{T} shape in the signal region data after the $\Delta\phi_{\ell\ell}$ requirement (see Section 6). The signal sensitivity for a SM Higgs

mass hypothesis m_H can also be enhanced by selecting events with m_T in the range $0.75\,m_H < m_T < m_H$, and this additional selection is used later in this document to illustrate the background model and the observed excess. The signal-to-background ratios after this selection for a SM Higgs boson with $m_H = 125$ GeV, with the added m_T requirement, are about 0.14, 0.19, and 1.0 for the $H + 0$-jet, $H + 1$-jet, and $H + 2$-jet selections, respectively.

4 Background normalisation and control samples

For the $H + 0$-jet and $H + 1$-jet analyses, the leading backgrounds from SM processes producing two isolated high-p_T leptons are WW and top (in this note, "top" background always includes both $t\bar{t}$ and single top (tW, tb, and tqb) unless explicitly stated otherwise). These are estimated using partially data-driven techniques based on normalising the MC predictions to the data in control regions dominated by the relevant background source. The W+jets background is fully estimated from data for all jet multiplicities. Only the backgrounds from Drell-Yan, diboson processes other than WW, and the WW background for the $H + 2$-jet analysis are estimated using simulation.

The control and validation regions are defined by selections similar to those used in the signal region but with some criteria reversed or modified to obtain signal-depleted samples enriched in a particular background. The control regions for WW and top are used to normalise the corresponding backgrounds in the fit, which helps reduce the sensitivity of the background predictions to the systematic uncertainties detailed in Section 5. The normalisation and m_T shape of the W+jets background are also derived from a control region and extrapolated into the signal region using a "fake factor" defined below. Same-sign dilepton events are produced primarily by the W+jets, $W\gamma^{(*)}/WZ^{(*)}$ and $Z^{(*)}Z^{(*)}$ processes. These events are thus used as a validation region to check those background predictions. The term "validation region" distinguishes these regions from the control regions, which are used to directly normalise the corresponding backgrounds.

Some control regions have significant contributions from backgrounds other than the targeted one, which introduces dependencies among the background estimates. These correlations are fully incorporated in the profile likelihood used to test the background-only hypothesis (see Section 6). In the following subsections, each background estimate is described after any others on which it depends. Because of this, the largest background (WW) is described last.

4.1 W+jets estimation and the same-sign validation sample

The W+jets background contribution is estimated using a control sample of events in which one of the two leptons satisfies the identification and isolation criteria described in Section 3, and the other lepton (denoted "anti-identified") fails these criteria but satisfies a loosened selection. Anti-identified electrons satisfy loosened isolation requirements and must fail at least one electron identification requirement, which may be on the shower shape or track quality. For anti-identified muons, the calorimeter isolation requirement is loosened and the track isolation and transverse impact parameter requirements are removed. Further, the muon must not pass all of the muon identification criteria. Otherwise, events in this sample are required to pass all of the signal selection requirements. The dominant contribution to this background comes from W+jets events in which a jet produces an object which is reconstructed as a lepton. This object may be either a true electron or muon from the decay of a heavy quark, or else, in the case of electrons, a product of the fragmentation incorrectly reconstructed as an isolated electron candidate. The purity of W+jets events in the control region is about 90% in the electron channel and 70% in the muon channel.
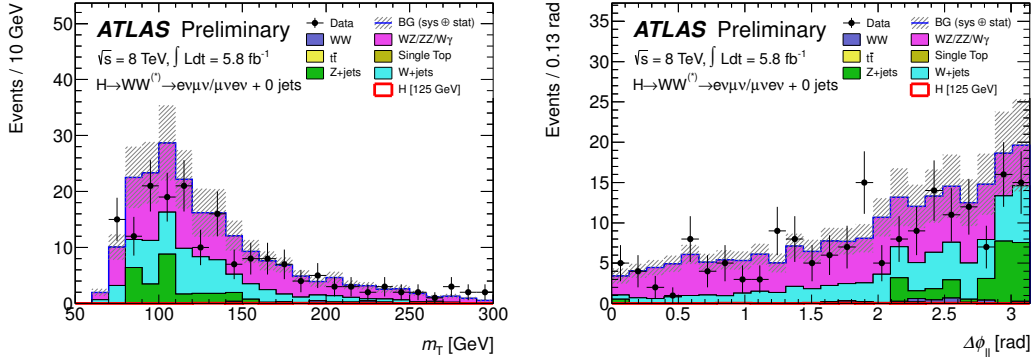
Figure 3: Distribution of m_T (left) and $\Delta\phi_{\ell\ell}$ (right) in the same-sign validation region after the $E_{T,rel}^{miss}$ and zero jet requirements. The lepton flavours are combined. The signal shown is for $m_H = 125$ GeV. The hashed area indicates the total uncertainty on the background prediction.

The W+jets background in the signal region is obtained by scaling the number of events in the data control sample by a "fake factor". The fake factor is defined as the ratio of the number of fully identified lepton candidates passing all selections to the number which are anti-identified. It is estimated as a function of the anti-identified lepton p_T using an inclusive dijet data sample, after subtracting the residual contributions from leptons produced by leptonic W and Z decays. For this subtraction, the W candidates are identified by requiring the transverse mass $m_T^W = \sqrt{2p_T^\ell E_T^{miss} \cdot (1 - \cos\Delta\phi)}$ to satisfy $m_T^W > 30$ GeV. In this expression, p_T^ℓ is the lepton transverse momentum and $\Delta\phi$ is the difference in azimuth between the lepton and $\mathbf{E}_T^{miss}$ directions. The Z candidates are identified as two opposite-sign leptons of the same flavour with $|m_{\ell\ell} - m_Z| < 15$ GeV, and need to be subtracted as part of the fake factor calculation even though only $e\mu$ candidates are selected in the signal region. The remaining lepton contamination, which includes $W\gamma$ and $W\gamma^*/WZ^{(*)}$ events, is subtracted using MC simulation.

The fake factor uncertainty is the main uncertainty on the W+jets background contribution. It is dominated by differences in jet composition between dijet and W+jets samples as observed in MC simulation, accounting also for differences between the heavy-flavour (b and c quark) content of the simulated W+jets events and what has been measured in data. The total systematic uncertainty on the fake factor also includes smaller contributions originating from trigger effects and the subtraction of the contamination from leptonic W and Z decays. The total relative uncertainty on this background is approximately 40% for the electron fakes and 40% for the muon fakes.

The processes producing the majority of same-sign dilepton events, W+jets, $W\gamma^{(*)}$, $WZ^{(*)}$, and $Z^{(*)}Z^{(*)}$ are all backgrounds to $H \to WW^{(*)} \to \ell\nu\ell\nu$. W+jets and $W\gamma^{(*)}$ are particularly important for the analysis optimised for a low Higgs boson mass hypothesis. Therefore the normalisation and kinematic features of same-sign dilepton events are used to validate these background predictions. Satisfactory agreement is observed overall, and example distributions, the m_T and $\Delta\phi_{\ell\ell}$ distributions of same-sign zero-jet events passing the preselection requirements, are shown in Fig. 3. The observed number of events is somewhat smaller than the estimated background, although the differences seen are well within the statistical and systematic uncertainties.

The $W\gamma$ background arises from the photon converting into a electron-positron pair, while the W decay provides the muon and the E_T^{miss} signatures. The simulation of the $W\gamma$ background is tested in a modified same-sign validation region in which the electron criteria that remove photon conversions are reversed. In this region, a high $W\gamma$ purity is obtained (approximately 80%). The final estimate is

taken from MC simulation since there are insufficient data in the $W\gamma$ validation region to derive an accurate normalisation, but the agreement between data and MC is good within the large statistical uncertainty.

4.2 Top-quark control sample

The number of background events from top quark production in the $H + 0$-jet signal region is normalised to the number of events satisfying the pre-selection criteria described in Section 3, namely, the selection up to but not including the jet multiplicity requirements. This sample is dominated by top quark events, as shown in Fig. 1. The small contribution of non-top backgrounds to this sample is estimated from simulation, except for the W+jets contribution, which is estimated from data. The fraction $f_{0-\text{jet}}^{\text{MC}}$ of top events in the preselected sample which pass the jet veto is initially estimated in simulation and then corrected using kinematic information from a second, b-tagged, control sample. Specifically, the correction uses the probability $P_1^{\text{b}-\text{tag}}$ for an event in the control sample to have no jets reconstructed in addition to the one that is tagged. Because b-tagging selects a nearly pure sample of top events, $P_1^{\text{b}-\text{tag}}$ can be calculated in both data and simulation. Then $f_{0-\text{jet}}^{\text{data}}$ is estimated by multiplying $f_{0-\text{jet}}^{\text{MC}}$ by the ratio $(P_1^{\text{b}-\text{tag,data}})^2/(P_1^{\text{b}-\text{tag,MC}})^2$, exploiting the stability of the ratio $f_{0-\text{jet}}/(P_1^{\text{b}-\text{tag}})^2$ with respect to experimental uncertainties and, to a lesser extent, assumptions about top event kinematics [67]. The efficiency for the remaining requirements on $p_{\text{T}}^{\ell\ell}$, $m_{\ell\ell}$, and $\Delta\phi_{\ell\ell}$ is taken from simulation. The ratio of the resulting prediction to the one from simulation alone is 1.11 ± 0.06 (stat). The total uncertainty on the estimate is 17%, which includes both statistical and systematic uncertainties, which are described in Section 5.

In the $H + 1$-jet and $H + 2$-jet analyses, the top quark background prediction is normalised to the data in a control sample defined by reversing the b-jet veto and removing the requirements on $\Delta\phi_{\ell\ell}$ and $m_{\ell\ell}$. Note that the $|\Delta y_{\text{jj}}|$ and m_{jj} requirements are included in the definition of the 2-jet control region. The resulting samples are primarily top events, and the small contribution from other sources is accounted for using simulation and the data-driven W+jets estimate. The predicted and observed dilepton transverse mass distributions of events in these samples are shown in Fig. 4. In these plots, a modified 2-jet control region, consisting of all events with two or more jets of which at least one is tagged, is used because there are not enough events in the full control region for a meaningful comparison of event kinematics. Good agreement is observed between data and MC for the numbers of events in the $H + 1$-jet and $H + 2$-jet control regions (see Table 2). The resulting normalisation factors are 1.11 ± 0.05 (stat) for the $H + 1$-jet analysis and 1.01 ± 0.26 (stat) for the $H + 2$-jet analysis. The total uncertainties on the estimated top-quark background in the $H + 1$-jet and $H + 2$-jet signal regions, including both statistical and systematic effects (which are described in Section 5), are 36% and 70%, respectively.

4.3 WW control sample

The WW background MC predictions in the $H + 0$-jet and $H + 1$-jet analyses, summed over lepton flavours, are normalised using control regions defined with the same selection as the signal region except that the $\Delta\phi_{\ell\ell}$ requirement is removed and the upper bound on $m_{\ell\ell}$ is replaced with a lower bound, $m_{\ell\ell} > 80$ GeV. The numbers of events in the WW control regions in the data agree well with the MC predictions, as can be seen in Table 2. Figure 5 shows the m_T shape predicted and observed for events in the WW control regions. Events from WW contribute about 70% of the total events in the zero jet control region and about 45% for the one jet control region. Good agreement
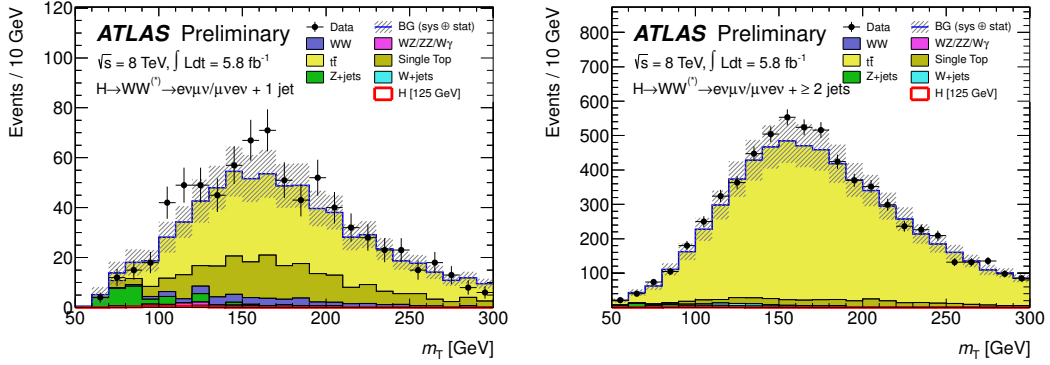
Figure 4: Distributions of the m_T variable in the $H+1$-jet (left) $H+2$-jet (right) top control regions. The lepton flavours are combined. The negligible signal shown is for $m_H = 125$ GeV. The $H+1$-jet top control region is identical to the $H+1$-jet signal region except that the veto on a b-tagged jet is reversed. The $H+2$-jet top control region used here is defined by the requirement of two or more jets, one of which is b-tagged jet, after the dilepton and $E_{T,rel}^{miss}$ preselection. It is larger than but contains the sample used to normalise the top background in the $H+2$-jet analysis. No data-driven normalisation factors are applied to the simulated data. The hashed area indicates the total uncertainty on the background prediction.

is observed between the predicted and observed distributions. Contributions from sources other than WW are derived as they are for the signal region, including the top and W+jets backgrounds. The resulting WW normalisation factors are 1.06 ± 0.06 (stat) for the $H+0$-jet channel and 0.99 ± 0.15 (stat) for the $H+1$-jet channel. The total uncertainty on the predicted WW background in the signal region, including both statistical and systematic effects (which are described in Section 5), is 13% for the $H+0$-jet analysis and 42% for the $H+1$-jet analysis. For the $H+2$-jet analysis, a signal-depleted region with a sufficient number of WW events to make a statistically accurate estimate of this background cannot be isolated and it is therefore predicted using simulation alone.

5 Systematic uncertainties

Theoretical uncertainties on the signal production cross sections are determined following Refs. [12, 68]. QCD factorisation and renormalisation scales are independently varied up and down by a factor of two. Independent uncertainties on the ggF signal production are assumed for the inclusive cross section and the cross section for production with at least one or two jets. The resulting uncertainties on the cross sections in exclusive jet multiplicity final states are taken into account, as well as anti-correlations caused by migrations between different jet multiplicities. The sum in quadrature of those uncertainties for $m_H = 125$ GeV amounts to 17% for the $H+0$-jet, and 36% for $H+1$-jet, final states [12, 68, 69]. The impact of the scale variations on both the VBF signal cross section and the jet veto acceptance, to which the $H+2$-jet analysis is mainly sensitive, is 4% [12]. Additional 7% uncertainties are included to account for the effect of the underlying event modelling on the signal acceptance for VBF signal events after jet tagging and central jet veto cuts. In the $H+2$-jet analysis, approximately 25% of the signal events are produced via ggF, with a relative uncertainty of around 25%.

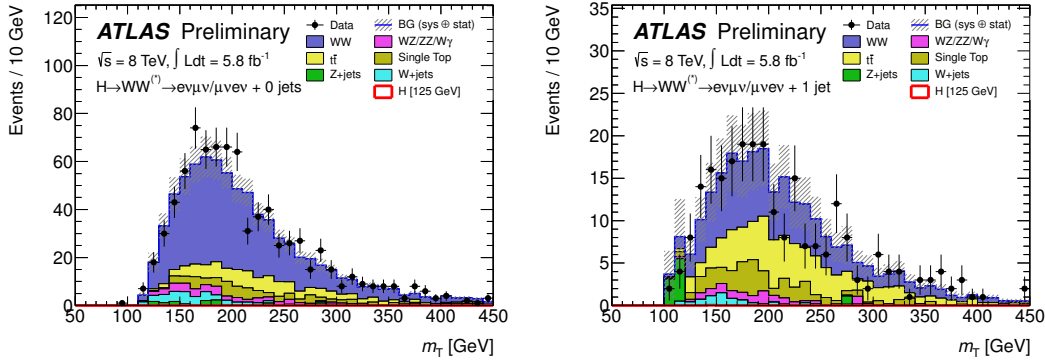PDF uncertainties are evaluated, following Refs. [39, 55, 70, 71], using the envelopes of error sets

Figure 5: m_T distributions in the WW control region in the H+0-jet (left) and H+1-jet (right) analyses. The lepton flavours are combined. The signal shown is for $m_H = 125$ GeV. The top backgrounds are scaled using the normalisation derived from the corresponding control regions described in the text. The hashed area indicates the total uncertainty on the background prediction.

as well as different PDF sets, applied separately to quark-quark, quark-gluon, and gluon-gluon initiated processes. For $m_H = 125$ GeV the relative PDF uncertainty is 8% for the ggF process and 2% for the VBF process. Uncertainties on the modelling of signal processes are estimated by using alternative generators, such as MC@NLO for the acceptance for the ggF process. As described in Section 4, the WW background is normalised to signal-free control regions. The theoretical uncertainty on the extrapolation to the signal region from the control regions has been evaluated according to the prescription of [12]. An additional modelling uncertainty is added to take into account differences in the number of extrapolated events obtained with MC@NLO+HERWIG and POWHEG+PYTHIA8. The uncertainties associated with the underlying event and parton showering are included in the acceptance uncertainty, although they are negligible compared to the scale uncertainties on the cross sections for H + 0-jet and H + 1-jet.

Uncertainties on the $W\gamma$ background normalisation are evaluated for each jet bin using the procedure described in [68]. The uncertainty relative to the predicted $W\gamma$ background is 11% for the 0-jet bin and 50% for the 1-jet bin. For $W\gamma^*$ with $m_{\ell\ell} < 7$ GeV, a K-factor of 1.3 ± 0.3 is applied to the MadGraph LO prediction based on the comparison with the MCFM NLO calculation. The corresponding K-factor and uncertainty for $WZ^{(*)}$ with $m_{\ell\ell} > 7$ GeV is 1.51 ± 0.45.

The main experimental uncertainties are related to the jet energy scale, which is determined from a combination of test beam, simulation, and *in situ* measurements. The uncertainty on the jet energy scale varies from 2% to 9% as a function of jet p_T and η for jets with $p_T > 25$ GeV and $|\eta| < 4.5$ [72]. An additional contribution to the jet energy scale uncertainty arises from pile-up, and is is estimated to vary between 1% and 5% for in-time pile-up, and up to 10% for out-of-time pile-up. The jet energy resolution varies from 7% to 22% as a function of jet p_T and η, and the relative systematic uncertainty on it, determined from *in situ* measurements, ranges from 17% to 25%. The reconstruction, identification, and trigger efficiencies for electrons and muons, as well as their momentum scales and resolutions, are estimated using $Z \to \ell\ell$, $J/\psi \to \ell\ell$, and $W \to \ell\nu$ decays ($\ell = e, \mu$). With the exception of the uncertainty on the electron selection efficiency, which varies between 2% and 5% as a function of p_T and η, the resulting uncertainties are all smaller than 1%. Jet energy scale and lepton momentum scale uncertainties are propagated to the E_T^{miss} computation. Additional contributions arise from jets with $p_T < 20$ GeV as well as from low-energy calorimeter deposits not associated with reconstructed physics objects [61]; their effect on the total signal and background yields is about 3%. The efficiency

of the b-tagging algorithm is calibrated using samples containing muons reconstructed in the vicinity of jets [64]. The resulting uncertainty on the b-jet tagging efficiency varies between 5% and 18% as a function of jet p_T. The preliminary uncertainty on the integrated luminosity is 3.6%, based on the calibration described in Ref. [73, 74].

For the backgrounds normalised using control regions, the systematic uncertainties are evaluated on the relative normalisation between the backgrounds in the signal and control regions and on the m_T shape in the signal region. The uncertainty on the top background in the $H + 0$-jet analysis is dominated by the size of neglected interference effects between $t\bar{t}$ and single top and by the impact of the choice of jet thresholds on top event kinematics. Systematic uncertainties are evaluated for the control regions described in Section 4 in the same way as for the signal regions.

In this analysis, a fit to the m_T distribution is performed in order to obtain the signal yield for each mass hypothesis. The m_T shapes for the individual backgrounds and signal do not exhibit a statistically significant dependence on the majority of the theoretical and experimental uncertainties. The remaining uncertainties that do produce statistically significant variations of the m_T shape have no appreciable effect on the final results, with the exception of the WW background, where an uncertainty is included to take into account differences in the m_T shape observed between the MC@NLO and POWHEG generators. However, the uncertainty on the shape of the total background is dominated by the uncertainties on the normalisations of the individual backgrounds.

6   Results

6.1   Results from the 8 TeV data

The expected numbers of signal (m_H = 125 GeV) and background events at several stages of the selection are presented in Table 2. The rightmost column shows the observed numbers of events in the data. The uncertainties shown include only the statistical uncertainties on the predictions from simulation. After all selection criteria, the dominant background in the $H + 0$-jet channel comes from continuum WW production, with smaller contributions from top, non-WW diboson, and W+jets events. In the $H+1$-jet and $H+2$-jet channels, the WW and top backgrounds are comparable. Figure 6 shows the distributions of the transverse mass after all selection criteria in the $H + 0$-jet and $H + 1$-jet analyses, for both lepton channels combined. No distributions are shown for the $H + 2$-jet channel because only two events in the data pass all of the selection through the $\Delta\phi_{\ell\ell}$ requirement.

Figure 7 shows the transverse mass distributions in data after all selection criteria have been applied, with the total estimated background subtracted. The $H+0$-jet and $H+1$-jet channels are summed and the predicted m_H = 125 GeV signal is superimposed. No systematic uncertainties are included.

Table 3 shows the numbers of events expected from signal and background and observed in data, after application of all selection criteria. To reflect better the sensitivity of the analysis, additional thresholds on m_T have been applied: $0.75\, m_H < m_T < m_H$ for m_H = 125 GeV. The results are shown for the $e\mu$ and μe channels combined. The uncertainties shown in Table 3 include the systematic uncertainties discussed in Section 5, constrained by the use of the control regions discussed in Section 4. The uncertainties are those that enter into the fitting procedure described below. An excess of events relative to the predicted background is observed in the data. Table 4 shows the magnitude of the main sources of systematic uncertainty on the signal (m_H = 125 GeV) and background predictions for the $H + 0$-jet and $H + 1$-jet analyses. Similarly to Table 3, the additional m_T cut is applied and the constraints from control regions are included.

The statistical analysis of the data employs a binned likelihood function $\mathcal{L}(\mu, \boldsymbol{\theta})$ constructed as the product of Poisson probability terms in each lepton flavour channel. The m_H-dependent m_T thresholds

Table 2: The expected numbers of signal and background events after the requirements listed in the first column, as well as the observed numbers of events. The signal is shown for $m_H = 125$ GeV. The W+jets background is estimated entirely from data, whereas MC predictions normalised to data in control regions are used for the WW, $t\bar{t}$, and $tW/tb/tqb$ processes in all the stages of the selection. Contributions from other background sources are taken entirely from MC predictions. The expected numbers of signal and background events, and the observed numbers of events, are shown also in the control regions. For these rows, the W+jets contribution is still taken from the data-driven estimate but no normalisation factors are applied, except that the top normalisation factor is applied for the top background estimate in the WW control regions. The bottom part of the table lists the number of expected and observed events after the $\Delta\phi_{\ell\ell}$ cut separated by the flavour of the subleading lepton. Only statistical uncertainties associated with the number of events in the MC samples are shown.

Cutflow evolution in the different signal regions									
$H + 0$-jet	Signal	WW	$WZ/ZZ/W\gamma$	$t\bar{t}$	$tW/tb/tqb$	$Z/\gamma^* +$ jets	$W +$ jets	Total Bkg.	Obs.
Jet Veto	47.5 ± 0.4	1308 ± 9	125 ± 4	184 ± 4	109 ± 6	850 ± 32	138 ± 4	2714 ± 34	2691
$p_T^{\ell\ell} > 30$ GeV	43.4 ± 0.4	1077 ± 8	99 ± 4	165 ± 4	98 ± 5	47 ± 8	102 ± 2	1589 ± 14	1664
$m_{\ell\ell} < 50$ GeV	34.9 ± 0.4	244 ± 4	33 ± 2	28 ± 2	17 ± 2	5 ± 2	29 ± 1	356 ± 6	421
$\Delta\phi_{\ell\ell} < 1.8$	33.6 ± 0.4	234 ± 4	32 ± 2	27 ± 2	17 ± 2	4 ± 2	25 ± 1	339 ± 6	407
$H + 1$-jet	Signal	WW	$WZ/ZZ/W\gamma$	$t\bar{t}$	$tW/tb/tqb$	$Z/\gamma^* +$ jets	$W +$ jets	Total Bkg.	Obs.
1 jet	24.9 ± 0.3	396 ± 5	74 ± 3	1652 ± 12	479 ± 12	283 ± 20	68 ± 3	2953 ± 27	2874
b-jet veto	21.1 ± 0.3	334 ± 4	56 ± 2	349 ± 6	115 ± 6	236 ± 18	53 ± 2	1144 ± 21	1115
$|\mathbf{p}_T^{tot}| < 30$ GeV	12.2 ± 0.2	210 ± 3	30 ± 2	139 ± 4	63 ± 5	124 ± 14	23 ± 2	590 ± 15	611
$Z \to \tau\tau$ veto	12.2 ± 0.2	204 ± 3	29 ± 2	133 ± 3	61 ± 5	98 ± 12	23 ± 2	547 ± 14	580
$m_{\ell\ell} < 50$ GeV	9.2 ± 0.2	37 ± 1	10 ± 1	21 ± 1	12 ± 2	16 ± 5	8.0 ± 0.9	104 ± 6	122
$\Delta\phi_{\ell\ell} < 1.8$	8.6 ± 0.2	34 ± 1	9 ± 1	20 ± 1	11 ± 2	3 ± 2	6.4 ± 0.7	84 ± 4	106
$H + 2$-jet	Signal	WW	$WZ/ZZ/W\gamma$	$t\bar{t}$	$tW/tb/tqb$	$Z/\gamma^* +$ jets	$W +$ jets	Total Bkg.	Obs.
≥ 2 jets	14.5 ± 0.2	139 ± 3	30 ± 2	7039 ± 24	376 ± 11	104 ± 12	71 ± 4	7759 ± 29	7845
b-jet veto	9.6 ± 0.2	95 ± 2	19 ± 1	356 ± 6	44 ± 4	62 ± 9	21 ± 2	597 ± 12	667
$|\Delta Y_{jj}| > 3.8$	2.0 ± 0.1	8.3 ± 0.6	2.0 ± 0.4	31 ± 2	5 ± 1	4 ± 2	1.4 ± 0.5	52 ± 3	44
Central jet veto (20 GeV)	1.6 ± 0.1	6.5 ± 0.5	1.3 ± 0.3	16 ± 1	4 ± 1	1 ± 1	0.5 ± 0.3	29 ± 2	22
$m_{jj} > 500$ GeV	1.1 ± 0.0	3.2 ± 0.4	0.7 ± 0.2	6.2 ± 0.7	1.8 ± 0.6	0.0 ± 0.0	0.0 ± 0.2	12 ± 1	13
$|\mathbf{p}_T^{tot}| < 30$ GeV	0.8 ± 0.0	1.7 ± 0.3	0.3 ± 0.1	2.5 ± 0.5	0.8 ± 0.4	0.0 ± 0.0	0.0 ± 0.2	5.4 ± 0.7	6
$Z \to \tau\tau$ veto	0.7 ± 0.0	1.8 ± 0.3	0.3 ± 0.1	2.4 ± 0.4	0.8 ± 0.4	0.0 ± 0.0	0.0 ± 0.2	5.2 ± 0.7	6
$m_{\ell\ell} < 80$ GeV	0.7 ± 0.0	0.6 ± 0.2	0.1 ± 0.1	0.8 ± 0.3	0.3 ± 0.2	0.0 ± 0.0	0.0 ± 0.2	1.9 ± 0.5	3
$\Delta\phi_{\ell\ell} < 1.8$	0.6 ± 0.0	0.5 ± 0.2	0.1 ± 0.1	0.5 ± 0.3	0.3 ± 0.2	0.0 ± 0.0	0.0 ± 0.2	1.4 ± 0.4	2

Composition of main control regions									
	Signal	WW	$WZ/ZZ/W\gamma$	$t\bar{t}$	$tW/tb/tqb$	$Z/\gamma^* +$ jets	$W +$ jets	Total Bkg.	Obs.
WW 0-jet	0.3 ± 0.0	531 ± 5	43 ± 2	104 ± 3	62 ± 4	11 ± 4	38 ± 1	789 ± 9	820
WW 1-jet	0.1 ± 0.0	112 ± 3	13 ± 1	80 ± 3	34 ± 3	9 ± 4	7.7 ± 0.8	256 ± 6	255
Top 1-jet	2.2 ± 0.1	39 ± 2	10 ± 1	489 ± 6	195 ± 7	28 ± 7	7 ± 1	768 ± 12	840
Top 2-jet	4.9 ± 0.1	45 ± 2	11.7 ± 1.0	6371 ± 23	315 ± 10	45 ± 8	52 ± 3	6840 ± 26	7178

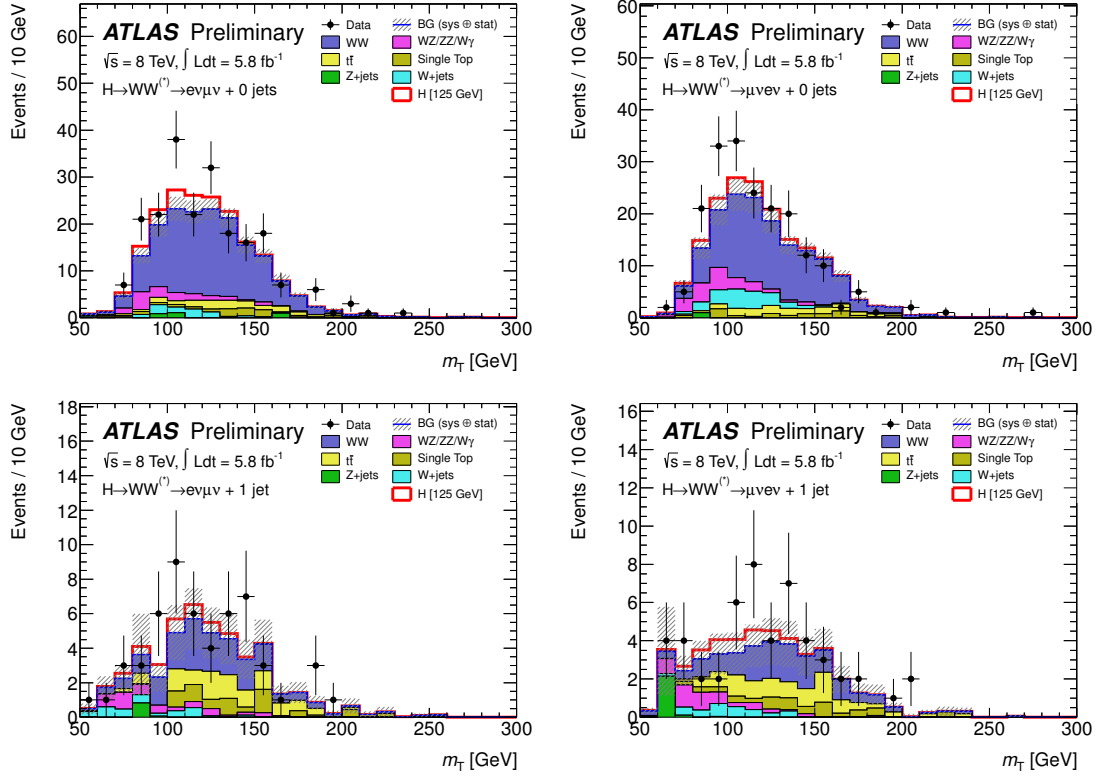| Signal region yield for $e\mu$ and μe channels separately				
	0-jet $e\mu$	0-jet μe	1-jet $e\mu$	1-jet μe
Total bkg.	177 ± 4	162 ± 4	43 ± 2	40 ± 3
Signal	18.7 ± 0.3	14.9 ± 0.2	4.3 ± 0.1	4.2 ± 0.1
Observed	213	194	54	52

13

Figure 6: Transverse mass, m_T, distribution in the $H + 0$-jet (top) and $H + 1$-jet (bottom) channels, for events satisfying all criteria. The plots on the left show the events with a subleading muon, and the plots on the right show the events with a subleading electron. The expected signal for a SM Higgs boson with $m_H = 125$ GeV is added on top of the estimated total background. The W+jets background is estimated directly from data and WW and top backgrounds are scaled to use the normalisation derived from the corresponding control regions described in the text. The hashed area indicates the total uncertainty on the background prediction.

Table 3: The expected numbers of signal ($m_H = 125$ GeV) and background events after the full selections, including a cut on the transverse mass of $0.75 \, m_H < m_T < m_H$ for $m_H = 125$ GeV. The observed numbers of events are also displayed. The uncertainties shown are the combination of the statistical and all systematic uncertainties, taking into account the constraints from control samples. These results differ from those given in Table 2 due to the application of the additional m_T cut. All numbers are summed over lepton flavours. For the $H + 2$-jet analysis, backgrounds with fewer than 0.01 events expected are marked as negligible using a '-'.

	Signal	WW	$WZ/ZZ/W\gamma$	$t\bar{t}$	$tW/tb/tqb$	$Z/\gamma^* +$ jets	$W +$ jets	Total Bkg.	Obs.
$H + 0$-jet	20 ± 4	101 ± 13	12 ± 3	8 ± 2	3.4 ± 1.5	1.9 ± 1.3	15 ± 7	142 ± 16	185
$H + 1$-jet	5 ± 2	12 ± 5	1.9 ± 1.1	6 ± 2	3.7 ± 1.6	0.1 ± 0.1	2 ± 1	26 ± 6	38
$H + 2$-jet	0.34 ± 0.07	0.10 ± 0.14	0.10 ± 0.10	0.15 ± 0.10	-	-	-	0.35 ± 0.18	0

described above are not used. Instead, the m_T distribution of events satisfying all of the criteria up to and including the $\Delta\phi_{\ell\ell}$ requirement is fit using the binned likelihood, with the $H + 0$-jet ($H +$
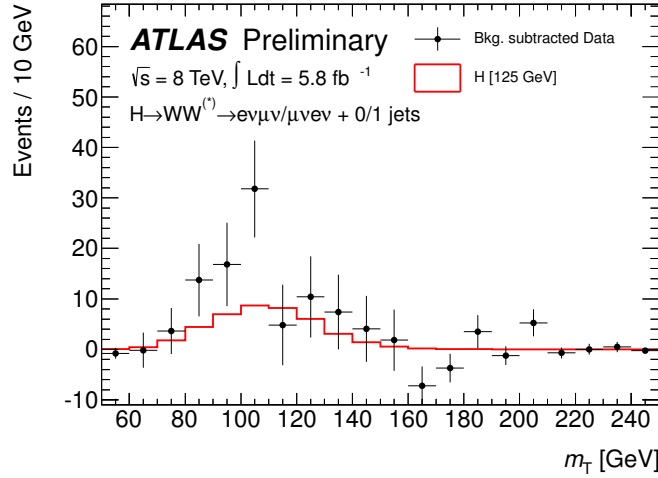
14

Figure 7: The m_T distribution in data with the estimated background subtracted, overlaid with the predicted signal for $m_H = 125$ GeV. The distributions are summed for the $H + 0$-jet and $H + 1$-jet analyses. The statistical errors of both the data and the subtracted background are reflected in the data points. The systematic uncertainty on the background estimate is not included.

1-jet) signal regions subdivided into five (three) m_T bins. For the $H + 2$-jet signal region, and the WW and top control regions, only the results integrated over m_T are used; no shape information is used due to the small number of events remaining after the event selection. The use of the m_T fit in place of a selection of events in a range of m_T increases the sensitivity of the analysis but also incurs additional systematic uncertainties on the modelling of the shape of the m_T distribution for the backgrounds. These additional uncertainties are not included in Table 3, but they are small in comparison to the uncertainties on the normalisation. The potential impact of the interference between WW and Higgs diagrams [75] above a value of m_T corresponding to the Higgs mass was investigated and found to be negligible. A "signal strength" parameter μ multiplies the expected Standard Model Higgs boson production signal in each bin. Signal and background predictions depend on systematic uncertainties that are parametrised by nuisance parameters θ, which in turn are constrained using Gaussian functions. The expected signal and background event counts in each bin are functions of θ. The parametrisation is chosen such that the rates in each channel are log-normally distributed for a normally distributed θ. The test statistic q_μ is then constructed using the profile likelihood: $q_\mu = -2\ln\left(\mathcal{L}(\mu, \hat{\theta}_\mu)/\mathcal{L}(\hat{\mu}, \hat{\theta})\right)$, where $\hat{\mu}$ and $\hat{\theta}$ are the parameters that maximise the likelihood (with the constraint $0 \leq \hat{\mu} \leq \mu$), and $\hat{\theta}_\mu$ are the nuisance parameter values that maximise the likelihood for a given μ. This test statistic is used to compute the probability (p_0) that a background fluctuation is more signal-like than the observed data, and to calculate the exclusion limits following the modified frequentist method known as CL_s [76, 77].

Figure 8 shows the expected and observed p_0 value and the fitted signal strength μ over the range $110 < m_H < 190$ GeV, for the combined $H + 0$-jet, $H + 1$-jet and $H + 2$-jet analyses. An excess of events is observed over the expected background, reflected by a low observed p_0 and a fitted μ which deviates from zero. Due to the limited mass resolution for this analysis, the p_0 distribution is rather flat around $m_H = 125$ GeV. The value of p_0 at $m_H = 125$ GeV is 8×10^{-4}, corresponding to 3.1 standard deviations. The minimum value of p_0, found at $m_H = 120$ GeV, is 6×10^{-4}, which corresponds to 3.2 standard deviations. The significance exceeds three standard deviations for a possible signal within the mass range $110 - 130$ GeV. The expected p_0 for a Higgs with $m_H = 125$ GeV is 0.05

15

Table 4: Main systematic uncertainties on the predicted numbers of signal (m_H = 125 GeV) and background events for the $H+$ 0-jet and $H+$ 1-jet analyses, relative to the total signal and background expectations. The same m_T criteria as in Table 3 are imposed. All numbers are summed over lepton flavours. The effect of the quoted inclusive signal cross section renormalisation and factorisation scale uncertainties on exclusive jet multiplicities is explained in Section 5. Sources of uncertainty that are negligible or not applicable in a particular column are marked with a '-'.

Source (0-jet)	Signal (%)	Bkg. (%)
Inclusive ggF signal ren./fact. scale	13	-
1-jet incl. ggF signal ren./fact. scale	10	-
Parton distribution functions	8	2
Jet energy scale	7	4
WW normalisation	-	7
WW modelling and shape	-	5
W+jets fake factor	-	5
QCD scale acceptance	4	2
Source (1-jet)	**Signal (%)**	**Bkg. (%)**
1-jet incl. ggF signal ren./fact. scale	28	-
WW normalisation	0	25
2-jet incl. ggF signal ren./fact. scale	16	-
b-tagging efficiency	-	10
Parton distribution functions	7	1
W+jets fake factor	0	5

or 1.6 standard deviations. The fitted signal strength is also shown in Figure 8 and is $\mu = 1.9 \pm 0.7$ at m_H = 126 GeV, the location of the minimum observed p_0 in the most recent ATLAS combined results [78]. The increase of the fitted signal strength at lower m_H is due to the decreasing expected $\sigma \cdot Br$ for the signal.

As a comparison, the p_0 was also evaluated using a counting experiment after applying a requirement on $0.75 \, m_H < m_T < m_H$, rather than fitting the m_T distribution (see Table 3 for event yields after the requirement on m_T has been applied for m_H = 125 GeV). The resulting decrease in sensitivity reduces the expected significance at m_H = 125 GeV to $p_0 = 0.07$ or 1.5 standard deviations. The observed significance in this variant of the analysis reaches a minimum of $p_0 = 2 \times 10^{-3}$, equivalent to 3.0 standard deviations, at m_H = 125 GeV.

The expected 95% CL_s limit on σ / σ_{SM} excludes a SM Higgs boson with a mass down to 129 GeV. However, due to the observed excess of events the observed excluded CL_s lower limit is only at 145 GeV.

6.2 Combination of the 7 TeV and 8 TeV results

The results obtained with the 5.8 fb^{-1} of 8 TeV data acquired in 2012 are combined with the published 4.7 fb^{-1} of 7 TeV results [13]. The 7 TeV analysis resulted in a signal strength of $\mu = 0.5 \pm 0.6$ at m_H = 126 GeV. The signal strengths measured with the 7 TeV and 8 TeV analyses separately are compatible within 1.5 standard deviations. Figure 9 shows the distribution of the transverse mass after all selection criteria have been applied, summed for the 7 TeV and 8 TeV data, after subtracting the total estimated background. The $H + 0$-jet and $H + 1$-jet channels are added and the predicted m_H = 125 GeV signal is superimposed. No systematic uncertainties are included. This figure is the equivalent of Figure 7 for the combined 2011 and 2012 datasets.

Figure 10 shows the expected and observed p_0 value and the fitted signal strength for the $H+0$-jet,
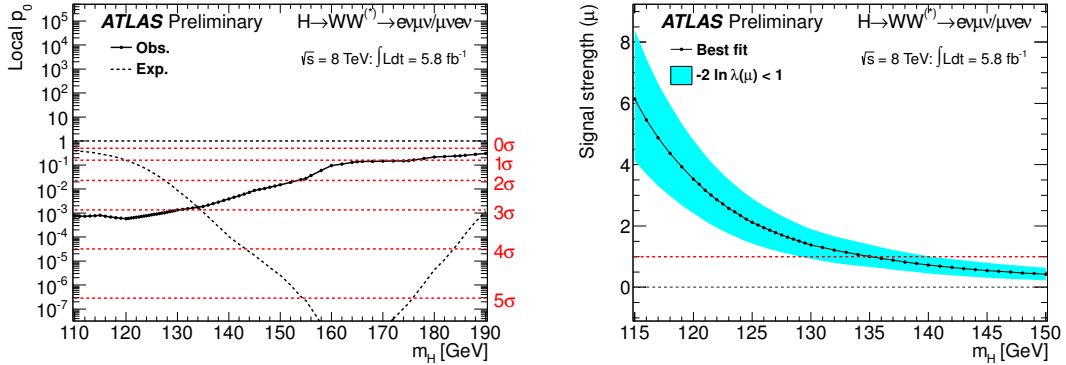
Figure 8: 2012 results, using 5.8 fb^{-1} of 8 TeV data. Left: observed (solid line) probability for the background-only scenario as a function of m_H. The dashed line shows the corresponding expectation for the signal+background hypothesis at the given value of m_H. Right: fitted signal strength parameter (μ) as a function of m_H for the low mass range.

$H+$ 1-jet and $H+$ 2-jet analyses with 7 TeV and 8 TeV data combined. Also shown is the expected distribution in the presence of a Higgs boson with $m_H = 125$ GeV. An excess of events is observed over the expected background, reflected by a low observed p_0 and a fitted μ which deviates from zero. The minimum value observed for p_0, found at $m_H = 125$ GeV, is 3×10^{-3}, corresponding to 2.8 standard deviations. The expected p_0 for a Higgs with $m_H = 125$ GeV is 0.01, or 2.3 standard deviations, for the combined 7 TeV and 8 TeV data. The fitted signal strength at $m_H = 126$ GeV is $\mu = 1.3 \pm 0.5$.

Figure 11 shows the two-dimensional likelihood contours for a simultaneous scan of μ and m_H, for this analysis and also for the $H \rightarrow ZZ^{(*)} \rightarrow 4\ell$ [79] and $H \rightarrow \gamma\gamma$ [80] analyses. The lack of mass resolution in the $H \rightarrow WW^{(*)} \rightarrow \ell\nu\ell\nu$ final state for low m_H can be seen clearly in contrast to the $H \rightarrow ZZ^{(*)} \rightarrow 4\ell$ and $H \rightarrow \gamma\gamma$ final states, but the best-fit values of μ and m_H are in reasonable agreement for all three analyses.

Figure 12 shows the observed local p_0 from the combined 7 TeV and 8 TeV results, compared to the one expected in the presence of a signal at $m_H = 125$ GeV. The shape and normalisation of the p_0 curves as a function of m_H are in agreement.

The 95% CL_s limit on σ/σ_{SM} is expected to exclude a SM Higgs boson with a mass above 124 GeV with the combined 7 TeV and 8 TeV data in the absence of a signal. However, due to the observed excess of events the observed exclusion CL_s lower limit is found at 137 GeV. The CL_s limit is shown in Figure 12.

7 Conclusion

A search for the SM Higgs boson has been performed in the $H \rightarrow WW^{(*)} \rightarrow \ell\nu\ell\nu$ channel in the mass range between 110 and 190 GeV using a data sample corresponding to 5.8 fb^{-1} of pp collision data from the Large Hadron Collider at $\sqrt{s} = 8$ TeV recorded in 2012 with the ATLAS detector. For $m_H \lesssim 150$ GeV, an excess of events over the expected background is observed, with a minimum local p_0-value of 6×10^{-4} at $m_H = 120$ GeV, or 3.2 standard deviations. A combined analysis of the 2011 and 2012 data results in a minimum local p_0 at $m_H = 125$ GeV of 3×10^{-3}, or 2.8 standard deviations. The best fit signal strength at $m_H = 126$ GeV, the location of the minimum observed p_0 in the most recent ATLAS combined results [78], cross section, is 1.3 ± 0.5. Given the observation of a new boson
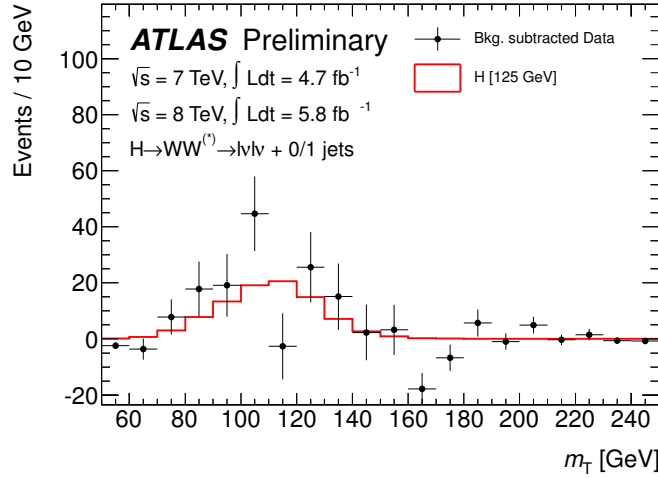
Figure 9: The m_T distribution in data with the estimated background subtracted, overlaid with the predicted signal for m_H = 125 GeV. The distributions are summed for the H + 0-jet and H + 1-jet analyses and the 7 TeV and 8 TeV data. The statistical errors of both the data and the subtracted background are reflected in the data points. The systematic uncertainty on the background estimate is not included.
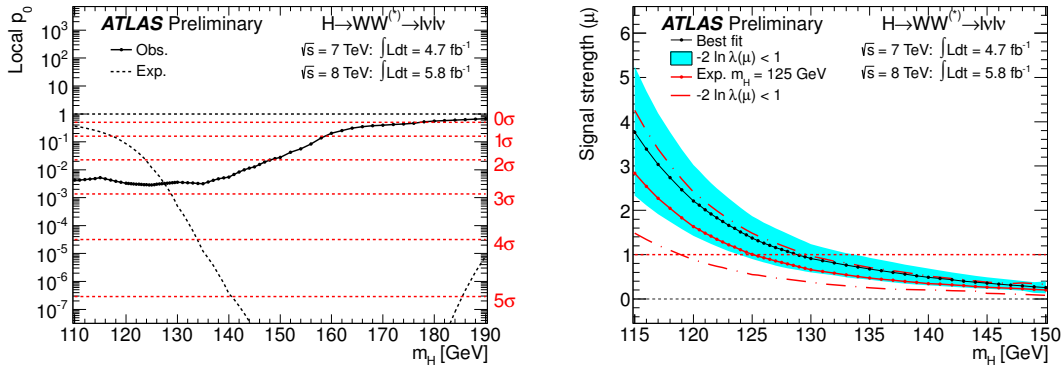

Figure 10: Combined 7 TeV and 8 TeV results. Left: observed (solid line) probability for the background-only scenario as a function of m_H. The dashed line shows the corresponding expectation for the signal+background hypothesis at the given value of m_H. Right: fitted signal strength parameter (μ) as a function of m_H for the low mass range (solid black line with cyan band). The expected result for a signal hypothesis of m_H = 125 GeV (red line) is included for comparison.

with mass close to 125 GeV in the $ZZ^{(*)}$ and $\gamma\gamma$ final states [79, 80], the excess observed in the $\ell\nu\ell\nu$ final state is consistent with the decay of this new particle into a pair of W bosons.
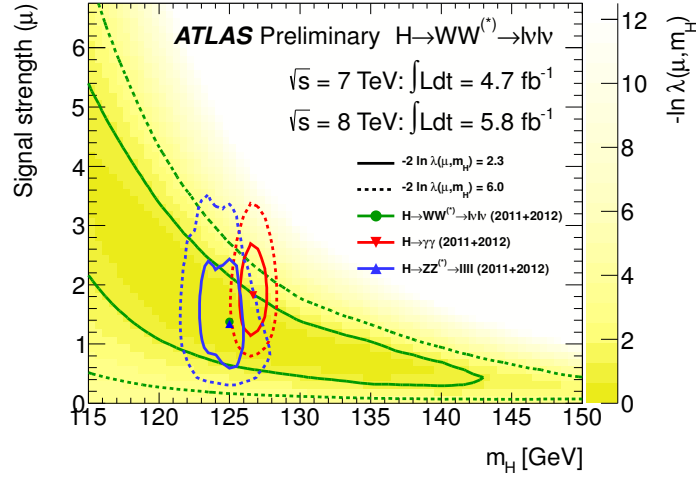
Figure 11: Approximate 68% and 95% two-dimensional likelihood ($\lambda(\mu, m_H)$) contours in the best-fit signal strength μ and m_H for the $WW^{(*)} \to \ell\nu\ell\nu$, $ZZ^{(*)} \to 4\ell$, and $\gamma\gamma$ analyses using the 2011 and 2012 data [81]. The yellow shading shows the $-\ln\lambda(\mu, m_H)$ values for $H \to WW^{(*)} \to \ell\nu\ell\nu$.
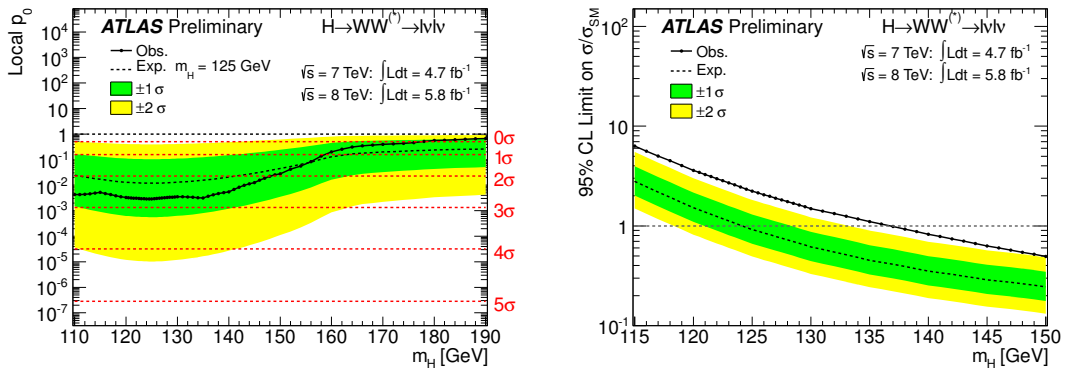
Figure 12: Left: Observed (solid line) probability for the background-only scenario, p_0, as a function of m_H, for the combined 7 TeV and 8 TeV data. The dashed line shows the corresponding expectation for the $m_H = 125$ GeV hypothesis. Right: Observed (solid) and expected (dashed) 95% CL upper limits on the cross section, normalised to the SM Higgs boson production cross section and as a function of m_H, over the full mass range considered in the 7 and 8 TeV combined data. Due to the excess of events observed in the low mass signal region, the corresponding mass points cannot be excluded as expected. The results at neighbouring mass points are highly correlated due to the limited mass resolution in this final state. The green and yellow regions indicate the $\pm 1\sigma$ and $\pm 2\sigma$ uncertainty bands on the expected p_0/limit, respectively.

References

[1] S. L. Glashow, *Partial symmetries of weak interactions*, Nucl. Phys. B **22** (1961) 579.

[2] S. Weinberg, *A model of leptons*, Phys. Rev. Lett. **19** (1967) 1264.

[3] A. Salam, *Elementary particle theory*. Almqvist and Wiksells, Stockholm, 1968.

[4] F. Englert and R. Brout, *Broken Symmetry and the Mass of Gauge Vector Mesons*, Phys. Rev. Lett. **13** (1964) 321.

[5] P. W. Higgs, *Broken Symmetries and the Masses of Gauge Bosons*, Phys. Rev. Lett. **13** (1964) 508.

[6] G. S. Guralnik, C. R. Hagen, and T. W. B. Kibble, *Global conservation laws and massless particles*, Phys. Rev. Lett. **13** (1964) 585.

[7] The ALEPH, DELPHI, L3, OPAL, SLD, CDF, and DØ Collaborations, and the LEP Tevatron SLD Electroweak Working Group. CERN-PH-EP-2010-095, 2010. `arXiv:1012.2367 [hep-ex]`.

[8] LEP Working Group for Higgs boson searches, *Search for the Standard Model Higgs boson at LEP*, Phys. Lett. B **565** (2003) 61, `arXiv:hep-ex/0306033`.

[9] Tevatron New Physics Higgs Working Group, CDF Collaboration, D0 Collaboration, *Updated Combination of CDF and D0 Searches for Standard Model Higgs Boson Production with up to 10.0 fb^{-1} of Data*, `arXiv:1207.0449 [hep-ex]`.

[10] ATLAS Collaboration, *Combined search for the Standard Model Higgs boson using up to 4.9 fb^{-1} of pp collision data at $\sqrt{s}$ = 7 TeV with the ATLAS detector at the LHC*, Phys. Lett. B **710** (2012) 49, `arXiv:1202.1408 [hep-ex]`.

[11] CMS Collaboration, *Combined results of searches for the Standard Model Higgs boson in pp collisions at $\sqrt{s}$ = 7 TeV*, Phys. Lett. B **710** (2012) 26, `arXiv:1202.1488 [hep-ex]`.

[12] LHC Higgs Cross Section Working Group, S. Dittmaier, C. Mariotti, G. Passarino, and R. Tanaka (Eds.), *Handbook of LHC Higgs cross sections: 2. Differential distributions*, `arXiv:1201.3084 [hep-ph]`.

[13] The ATLAS Collaboration, *Search for the Standard Model Higgs boson in the $H \to WW^{(*)} \to \ell\nu\ell\nu$ decay mode with 4.7 fb^{-1} of ATLAS data at $\sqrt{s}$ = 7 TeV*, arXiv:1206.0756, submitted to Phys. Lett. B (2012) .

[14] CMS Collaboration, *Search for the standard model Higgs boson decaying to W^+W^- in the fully leptonic final state in pp collisions at $\sqrt{s}$ = 7 TeV*, Phys. Lett. B **710** (2012) 91, `arXiv:1202.1489 [hep-ex]`.

[15] ATLAS Collaboration, *The ATLAS experiment at the CERN Large Hadron Collider*, JINST **3** (2008) S08003.

[16] D. de Florian et al., *Transverse-momentum resummation: Higgs boson production at the Tevatron and the LHC*, JHEP **11** (2011) 064, `arXiv:1109.2109 [hep-ph]`. For Higgs boson $p_\mathrm{T} > m_H$, the calculation is switched from NLO+NLL to NLO.

[17] P. S. E. Bagnaschi, G. Degrassi and A. Vicini, *Higgs production via gluon fusion in the POWHEG approach in the SM and in the MSSM*, JHEP **1202** (2012) 88, `arXiv:1111.2854` `[hep-ph]`.

[18] S. Alioli, P. Nason, C. Oleari, and E. Re, *NLO Higgs boson production via gluon fusion matched with shower in POWHEG*, JHEP **0904** (2009) 002, `arXiv:0812.0578` `[hep-ph]`.

[19] T. Sjostrand, S. Mrenna, and P. Z. Skands, *A Brief Introduction to PYTHIA 8.1*, CERN-LCGAPP **04** (2007) 1, `arXiv:0710.3820`.

[20] P. Nason and C. Oleari, *NLO Higgs boson production via vector-boson fusion matched with shower in POWHEG*, JHEP **1002** (2010) 037, `arXiv:0911.5299` `[hep-ph]`.

[21] S. Frixione and B. R. Webber, *Matching NLO QCD computations and parton shower simulations*, JHEP **0206** (2002) 029, `arXiv:hep-ph/0204244`.

[22] G. Corcella et al., *HERWIG 6: An event generator for hadron emission reactions with interfering gluons (including super-symmetric processes)* , JHEP **0101** (2001) 010.

[23] T. Binoth, M. Ciccolini, N. Kauer and M. Krämer, *Gluon-induced W-boson pair production at the LHC*, JHEP **0612** (2006) 046, `arXiv:hep-ph/0611170`.

[24] B. P. Kersevan and E. Richter-Was, *The Monte Carlo event generator AcerMC version 2.0 with interfaces to PYTHIA 6.2 and HERWIG 6.5*, `arXiv:hep-ph/0405247`.

[25] M. L. Mangano et al., *ALPGEN, a generator for hard multi-parton processes in hadronic collisions*, JHEP **0307** (2003) 001, `arXiv:hep-ph/0206293`.

[26] J. Alwall et al., *MadGraph/MadEvent v4: The new web generation*, JHEP **0709** (2007) 028, `arXiv:0706.2334` `[hep-ph]`.

[27] J. Alwall, M. Herquet, F. Maltoni, O. Mattelaer, and T. Stelzer, *MadGraph 5 : Going Beyond*, JHEP **1106** (2011) 128, `arXiv:1106.0522` `[hep-ph]`.

[28] T. Sjostrand, S. Mrenna, and P. Z. Skands, *PYTHIA 6.4 physics and manual*, JHEP **0605** (2006) 026, `arXiv:hep-ph/0603175`.

[29] R. C. Gray, C. Kilic, M. Park, S. Somalwar, and S. Thomas, *Backgrounds To Higgs boson searches from $W\gamma^* \to l\nu l(l)$ asymmetric internal conversion*, `arXiv:1110.1368` `[hep-ph]`.

[30] A. Bredenstein, A. Denner, S. Dittmaier, and M. M. Weber, *Precise predictions for the Higgs-boson decay $H \to WW/ZZ \to 4$ leptons*, Phys. Rev. D **74** (2006) 013004, `arXiv:hep-ph/0604011`.

[31] A. Bredenstein, A. Denner, S. Dittmaier, and M. Weber, *Radiative corrections to the semileptonic and hadronic Higgs-boson decays $H \to WW/ZZ \to 4$ fermions*, JHEP **0702** (2007) 080, `arXiv:hep-ph/0611234`.

[32] A. Djouadi, J. Kalinowski, and M. Spira, *HDECAY: A program for Higgs boson decays in the Standard Model and its supersymmetric extension*, Comput. Phys. Commun. **108** (1998) 56, `arXiv:hep-ph/9704448`.

21

[33] A. Djouadi, M. Spira, and P. M. Zerwas, *Production of Higgs bosons in proton colliders: QCD corrections*, Phys. Lett. B **264** (1991) 440.

[34] S. Dawson, *Radiative corrections to Higgs boson production*, Nucl. Phys. B **359** (1991) 283.

[35] M. Spira, A. Djouadi, D. Graudenz, and P. M. Zerwas, *Higgs boson production at the LHC*, Nucl. Phys. B **453** (1995) 17, `arXiv:hep-ph/9504378`.

[36] R. Harlander and W. B. Kilgore, *Next-to-next-to-leading order Higgs production at hadron colliders*, Phys. Rev. Lett. **88** (2002) 201801, `arXiv:hep-ph/0201206`.

[37] C. Anastasiou and K. Melnikov, *Higgs boson production at hadron colliders in NNLO QCD*, Nucl. Phys. B **646** (2002) 220, `arXiv:hep-ph/0207004`.

[38] V. Ravindran, J. Smith, and W. L. van Neerven, *NNLO corrections to the total cross section for Higgs boson production in hadron hadron collisions*, Nucl. Phys. B **665** (2003) 325, `arXiv:hep-ph/0302135`.

[39] A. D. Martin, W. J. Stirling, R. S. Thorne, and G. Watt, *Parton distributions for the LHC*, Eur. Phys. J. C **63** (2009) 189, `arXiv:0901.0002 [hep-ph]`.

[40] U. Aglietti, R. Bonciani, G. Degrassi, and A. Vicini, *Two loop light fermion contribution to Higgs production and decays*, Phys. Lett. B **595** (2004) 432, `arXiv:hep-ph/0404071`.

[41] S. Actis, G. Passarino, C. Sturm, and S. Uccirati, *NLO electroweak corrections to Higgs boson production at hadron colliders*, Phys. Lett. B **670** (2008) 12, `arXiv:0809.1301 [hep-ph]`.

[42] S. Catani, D. de Florian, M. Grazzini, and P. Nason, *Soft-gluon re-summation for Higgs boson production at hadron colliders*, JHEP **0307** (2003) 028, `arXiv:hep-ph/0306211`.

[43] C. Anastasiou, S. Buehler, F. Herzog, and A. Lazopoulos, *Inclusive Higgs boson cross-section for the LHC at 8 TeV*, JHEP **1204** (2012) 004, `arXiv:1202.3638 [hep-ph]`.

[44] D. de Florian and M. Grazzini, *Higgs production at the LHC: updated cross sections at $\sqrt{s} = 8$ TeV*, `arXiv:1206.4133 [hep-ph]`.

[45] P. Bolzoni, F. Maltoni, S.-O. Moch, and M. Zaro, *Higgs production via vector-boson fusion at NNLO in QCD*, Phys. Rev. Lett. **105** (2010) 011801, `arXiv:1003.4451 [hep-ph]`.

[46] M. Ciccolini, A. Denner, and S. Dittmaier, *Strong and electroweak corrections to the production of Higgs+2 jets via weak interactions at the LHC*, Phys. Rev. Lett. **99** (2007) 161803, `arXiv:0707.0381 [hep-ph]`.

[47] M. Ciccolini, A. Denner, and S. Dittmaier, *Electroweak and QCD corrections to Higgs production via vector-boson fusion at the LHC*, Phys. Rev. D **77** (2008) 013002, `arXiv:0710.4749 [hep-ph]`.

[48] K. Arnold, M. Bahr, G. Bozzi, F. Campanario, C. Englert, et al., *VBFNLO: A parton level Monte Carlo for processes with electroweak bosons*, Comput. Phys. Commun. **180** (2009) 1661, `arXiv:0811.4559 [hep-ph]`.

[49] T. Han and S. Willenbrock, *QCD correction to the $pp \to WH$ and ZH total cross sections*, Phys. Lett. B **273** (1991) 167.

[50] O. Brein, A. Djouadi, and R. Harlander, *NNLO QCD corrections to the Higgs-strahlung processes at hadron colliders*, Phys. Lett. B **579** (2004) 149, `arXiv:hep-ph/0307206`.

[51] M. L. Ciccolini, S. Dittmaier, and M. Kramer, *Electroweak radiative corrections to associated WH and ZH production at hadron colliders*, Phys. Rev. D **68** (2003) 073003, `arXiv:hep-ph/0306234`.

[52] J. M. Butterworth, J. R. Forshaw, and M. H. Seymour, *Multiparton interactions in photoproduction at HERA*, Z. Phys. **C72** (1996) 637, `arXiv:hep-ph/9601371`.

[53] J. Alwall et al., *Comparative study of various algorithms for the merging of parton showers and matrix elements in hadronic collisions*, Eur. Phys. J. C **53** (2008) 473, `arXiv:0706.2569 [hep-ph]`.

[54] J. M. Campbell and R. K. Ellis, *An update on vector boson pair production at hadron colliders*, Phys. Rev. D **60** (1999) 113006, `arXiv:hep-ph/9905386`.

[55] H.-L. Lai et al., *New parton distributions for collider physics*, Phys. Rev. D **82** (2010) 074024, `arXiv:1007.2241 [hep-ph]`.

[56] P. M. Nadolsky et al., *Implications of CTEQ global analysis for collider observables*, Phys. ReV. D **78** (2008) 013004, `arXiv:0802.0007 [hep-ph]`.

[57] ATLAS Collaboration, *The ATLAS simulation infrastructure*, Eur. Phys. J. C **70** (2010) 823, `arXiv:1005.4568 [physics.ins-det]`.

[58] S. Agostinelli et al., *GEANT 4, a simulation toolkit*, Nucl. Instrum. Meth. **A506** (2003) 250.

[59] ATLAS Collaboration, *Electron performance measurements with the ATLAS detector using the 2010 LHC proton-proton collision data*, Eur. Phys. J. C **72** (2012) 1909, `arXiv:1110.3174 [hep-ex]`.

[60] ATLAS Collaboration, *Muon reconstruction efficiency in reprocessed 2010 LHC proton-proton collision data recorded with the ATLAS detector*, ATLAS-CONF-2011-063 (2011) . https://cdsweb.cern.ch/record/1345743.

[61] ATLAS Collaboration, *Performance of missing transverse momentum reconstruction in proton-proton collisions at 7 TeV with ATLAS*, Eur. Phys. J. C **72** (2012) 1844, `arXiv:1108.5602 [hep-ex]`.

[62] M. Cacciari, G. P. Salam, and G. Soyez, *Anti-k_t jet clustering algorithm*, JHEP **0804** (2008) 063, `arXiv:0802.1189`.

[63] ATLAS Collaboration, *Commissioning of the ATLAS high-performance b-tagging algorithms in the 7 TeV collision data*, ATLAS-CONF-2011-102 (2011) . https://cdsweb.cern.ch/record/1369219.

[64] ATLAS Collaboration, *Measurement of the b-tag Efficiency in a Sample of Jets Containing Muons with 5 fb^{-1} of Data from the ATLAS Detector*, ATLAS-CONF-2012-043 (2012) . https://cdsweb.cern.ch/record/1435197.

[65] R.K. Ellis et al., *Higgs decay to $\tau^+\tau^-$: A possible signature of intermediate mass Higgs bosons at the SSC*, Nucl. Phys. B **297** (1988) 221.

[66] A. J. Barr, B. Gripaios, and C. G. Lester, *Measuring the Higgs boson mass in dileptonic W-boson decays at hadron colliders*, JHEP **0907** (2009) 072, arXiv:0902.4864 [hep-ph].

[67] B. Mellado, X. Ruan, and Z. Zhang, *Extraction of top backgrounds in the Higgs boson search with the $H \rightarrow WW^{\star} \rightarrow \ell\ell + E_{\mathrm{T}}^{\mathrm{miss}}$ decay with a full-jet veto at the LHC*, Phys. Rev. D **84** (2011) 096005, arXiv:1101.1383 [hep-ph].

[68] I. Stewart and F. Tackmann, *Theory uncertainties for Higgs mass and other searches using jet bins*, Phys. Rev. D **85** (2012) 034011, arXiv:1107.2117 [hep-ph].

[69] ATLAS and CMS Collaborations, *Procedure for the LHC Higgs boson search combination in summer 2011*, ATL-PHYS-PUB-2011-011, CMS-NOTE-2011-005 (2011) . https://cdsweb.cern.ch/record/1375842.

[70] M. Botje et al., *The PDF4LHC working group interim recommendations*, arXiv:1101.0538 [hep-ph].

[71] R. D. Ball, V. Bertone, F. Cerutti, L. D. Debbio, S. Forte, et al., *Impact of heavy quark masses on parton distributions and LHC phenomenology*, Nucl. Phys. B **849** (2011) 296, arXiv:1101.1300 [hep-ph].

[72] ATLAS Collaboration, *Jet energy measurement with the ATLAS detector in proton-proton collisions at $\sqrt{s} = 7$ TeV*, arXiv:1112.6426 [hep-ex]. Submitted to Eur. Phys. J. C.

[73] ATLAS Collaboration, *Luminosity Determination in pp Collisions at $\sqrt{s} = 7$ TeV Using the ATLAS Detector at the LHC*, Eur. Phys. J. C **71** (2011) 1630, arXiv:1101.2185 [hep-ex].

[74] ATLAS Collaboration, *Luminosity determination in pp collisions at $\sqrt{s} = 7$ TeV using the ATLAS detector in 2011*, ATLAS-CONF-2011-116 (2011) . https://cdsweb.cern.ch/record/1376384.

[75] J. M. Campbell, R. K. Ellis, and C. Williams, *Gluon-Gluon Contributions to W+ W- Production and Higgs Interference Effects*, JHEP **1110** (2011) 005, arXiv:1107.5569 [hep-ph].

[76] A.L. Read, *Presentation of search results: the CL_s technique*, J. Phys. G **28** (2002) 2693.

[77] G. Cowan, K. Cranmer, E. Gross, and O. Vitells, *Asymptotic formulae for likelihood-based tests of new physics*, Eur. Phys. J. C **71** (2011) 1554.

[78] ATLAS Collaboration, *Observation of a New Particle in the Search for the Standard Model Higgs Boson with the ATLAS Detector at the LHC*, arXiv:1207.7214, submitted to Phys. Lett. B (2012) .

[79] The ATLAS Collaboration, *Observation of an Excess of Events in the Search for the Standard Model Higgs Boson in the $H \rightarrow ZZ \rightarrow 4\ell$ Channel with the ATLAS detector*, ATLAS-CONF-2012-092 (2012) . https://cdsweb.cern.ch/record/1460411.

[80] The ATLAS Collaboration, *Observation of an Excess of Events in the Search for the Standard Model Higgs Boson in the $\gamma\gamma$ Channel with the ATLAS Detector*, ATLAS-CONF-2012-091 (2012) . https://cdsweb.cern.ch/record/1460410.

[81] The ATLAS Collaboration, *Observation of an Excess of Events in the Search for the Standard Model Higgs Boson with the ATLAS Detector at the LHC*, ATLAS-CONF-2012-093 (2012) . https://cdsweb.cern.ch/record/1460439.
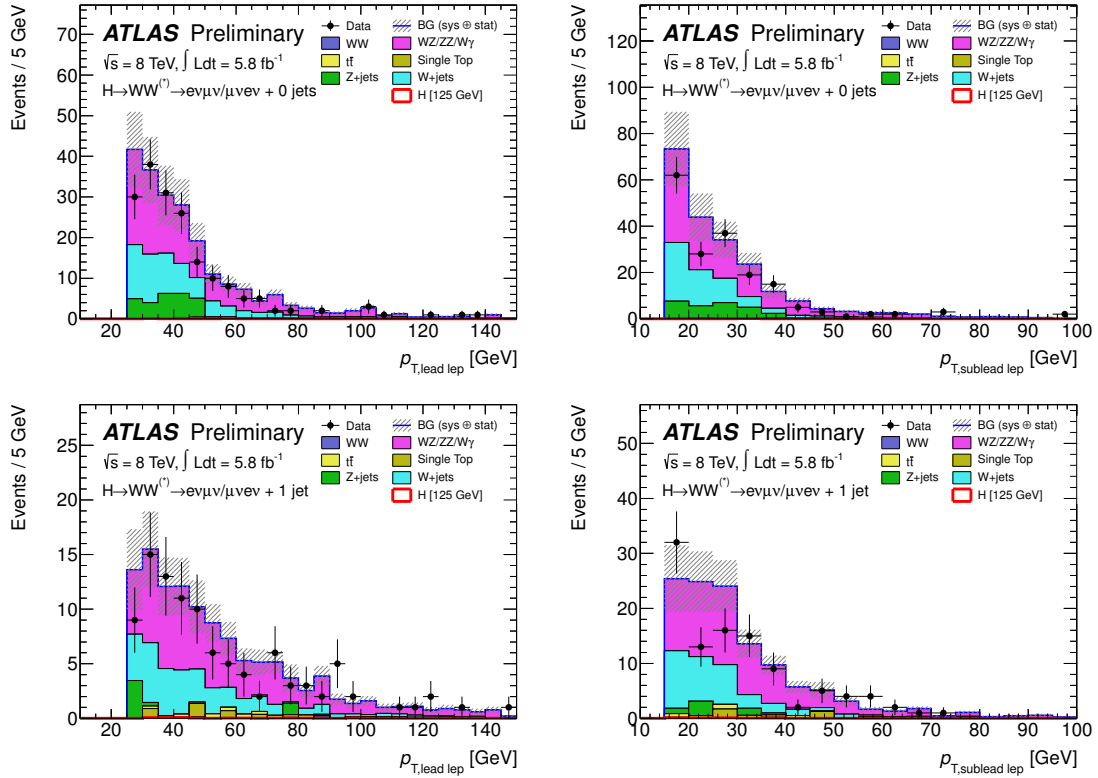
A Additional Figures

Figure 13: Distributions for the same-sign validation region; leading lepton p_T (top left) and sub-leading lepton p_T (top right) after the zero jet veto and leading lepton p_T (bottom left) and sub-leading lepton p_T (bottom right) after the one jet requirement. The $e\mu$ and μe channels are combined. The signal shown is for $m_H = 125$ GeV. The hashed area indicates the total uncertainty on the background prediction.
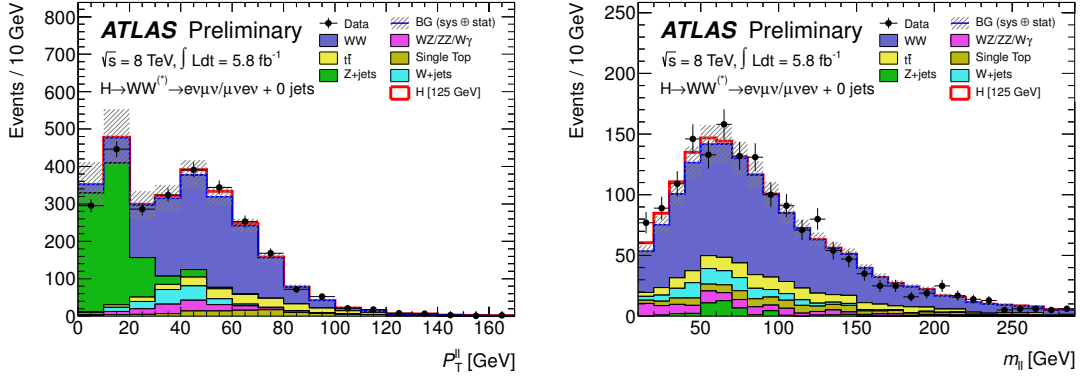
Figure 14: Kinematic distributions in the $H + 0$-jet channel. $p_T^{\ell\ell}$ after the zero jet veto (left), and $m_{\ell\ell}$ after the cut on $p_T^{\ell\ell}$ (right). The signal shown is added on top of the background and is for $m_H = 125$ GeV. The WW and top backgrounds are scaled to use the normalisation derived from the corresponding control regions described in the text. The hashed area indicates the total uncertainty on the background prediction.
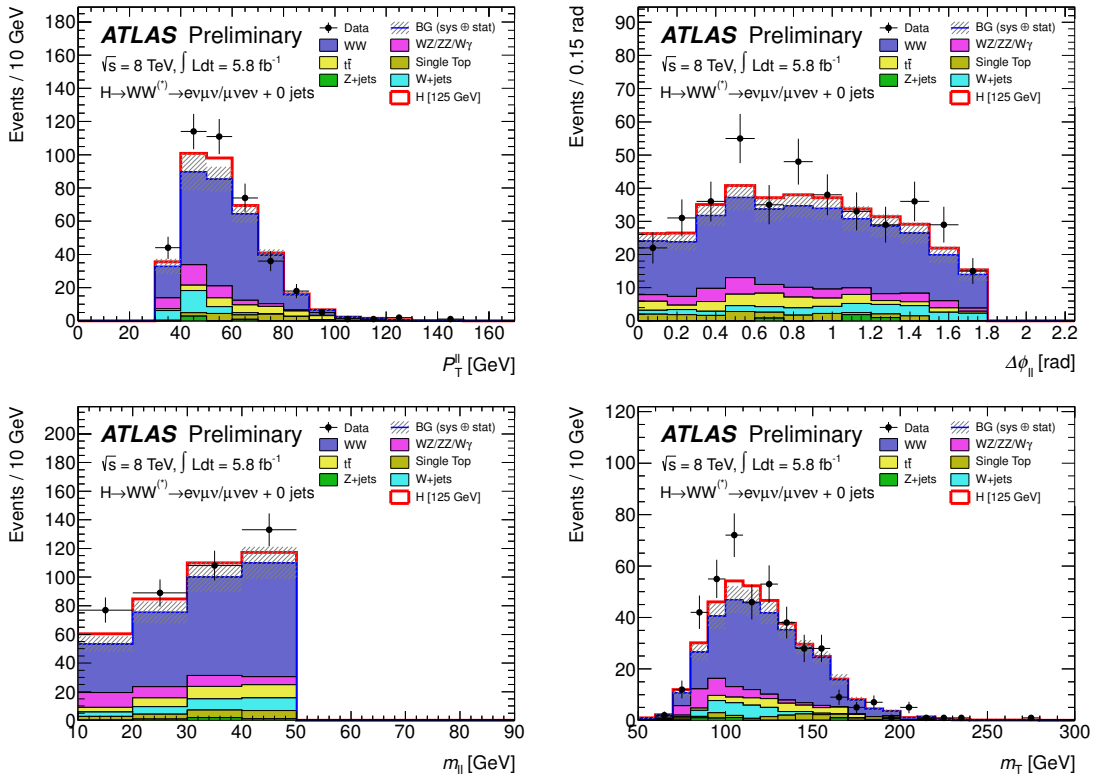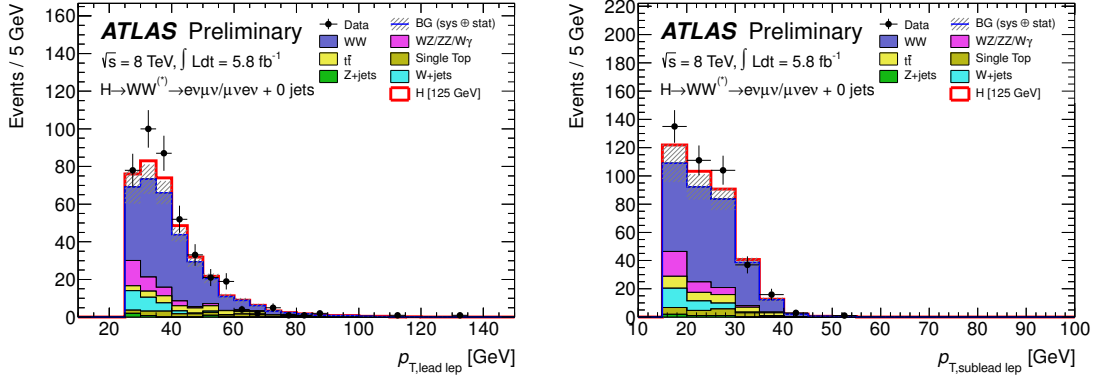

Figure 15: Kinematic distributions in the $H + 0$-jet channel after full selection ($\Delta\phi_{\ell\ell} < 1.8$): $p_T^{\ell\ell}$ (top left), $\Delta\phi_{\ell\ell}$ (top right), $m_{\ell\ell}$ (bottom left), and m_T (bottom right). The $e\mu$ and μe channels are combined. The signal shown is added on top of the background and is for $m_H = 125$ GeV. The WW and top backgrounds are scaled to use the normalisation derived from the corresponding control regions described in the text. The hashed area indicates the total uncertainty on the background prediction.

27

Figure 16: Kinematic distributions in the $H + 0$-jet channel after full selection ($\Delta\phi_{\ell\ell} < 1.8$): leading lepton p_T (left) and sub-leading lepton p_T (right). The $e\mu$ and μe channels are combined. The signal shown is added on top of the background and is for $m_H = 125$ GeV. The WW and top backgrounds are scaled to use the normalisation derived from the corresponding control regions described in the text. The hashed area indicates the total uncertainty on the background prediction.
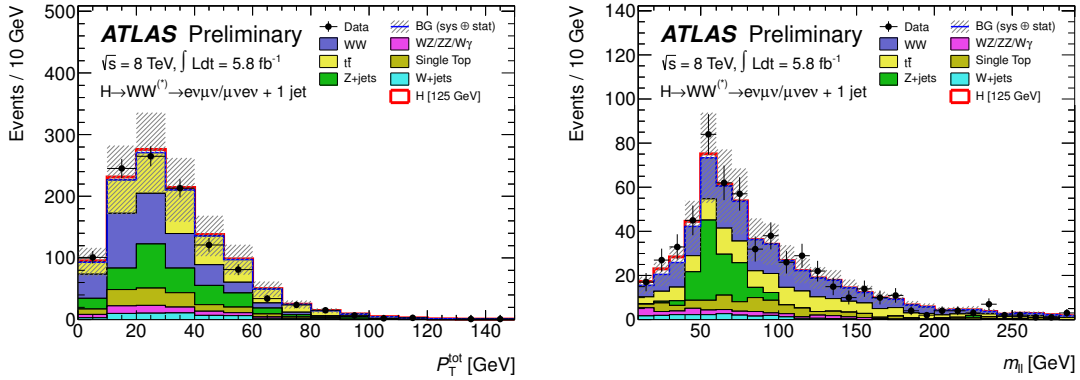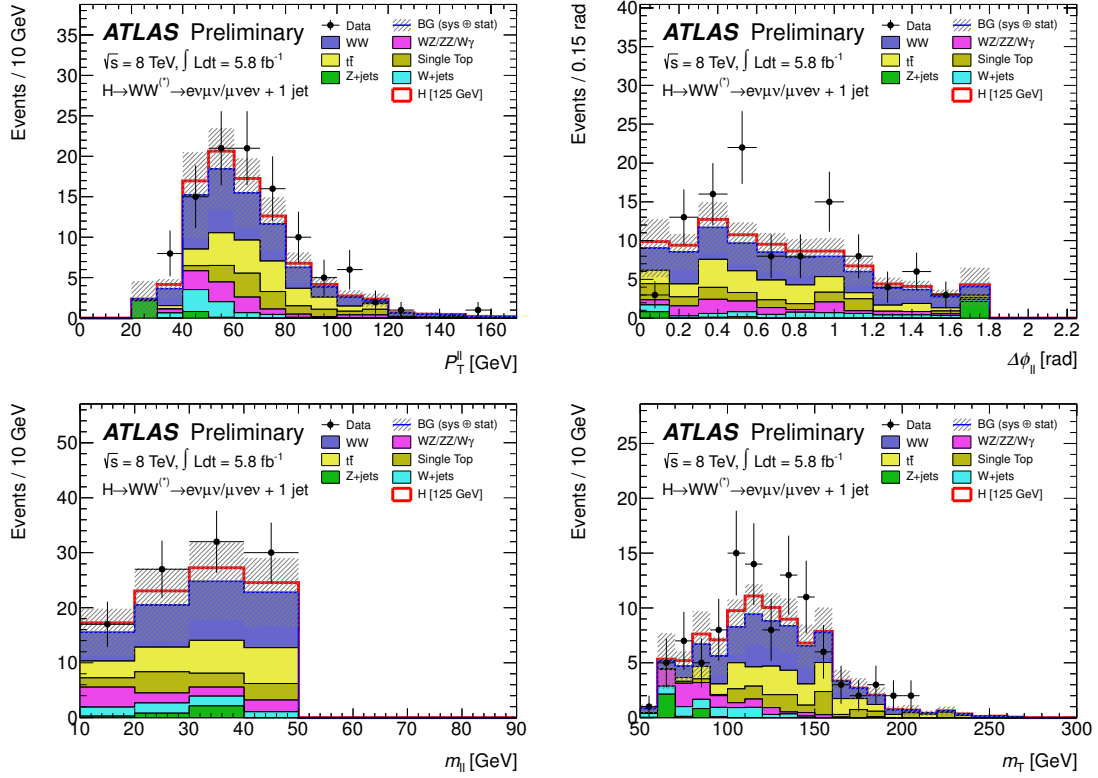

Figure 17: Kinematic distributions in the $H + 1$-jet channel. $|\mathbf{p}_T^{tot}|$ after the b-jet veto (left), and $m_{\ell\ell}$ after the $Z \to \tau\tau$ veto (right). The signal shown is added on top of the background and is for $m_H = 125$ GeV. The WW and top backgrounds are scaled to use the normalisation derived from the corresponding control regions described in the text. The hashed area indicates the total uncertainty on the background prediction.
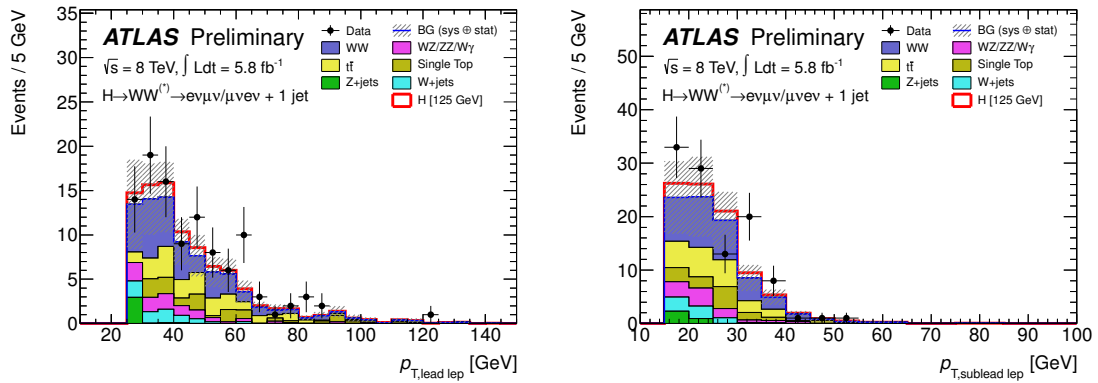
Figure 18: Kinematic distributions in the $H + 1$-jet channel after full selection ($\Delta\phi_{\ell\ell} < 1.8$): $p_T^{\ell\ell}$ (top left), $\Delta\phi_{\ell\ell}$ (top right), $m_{\ell\ell}$ (bottom left), and m_T (bottom right). The eμ and μe channels are combined. The signal shown is added on top of the background and is for $m_H = 125$ GeV. The WW and top backgrounds are scaled to use the normalisation derived from the corresponding control regions described in the text. The hashed area indicates the total uncertainty on the background prediction.

Figure 19: Kinematic distributions in the $H + 1$-jet channel after full selection ($\Delta\phi_{\ell\ell} < 1.8$): leading lepton p_T (left) and sub-leading lepton p_T (right). The $e\mu$ and μe channels are combined. The signal shown is added on top of the background and is for $m_H = 125$ GeV. The WW and top backgrounds are scaled to use the normalisation derived from the corresponding control regions described in the text. The hashed area indicates the total uncertainty on the background prediction.
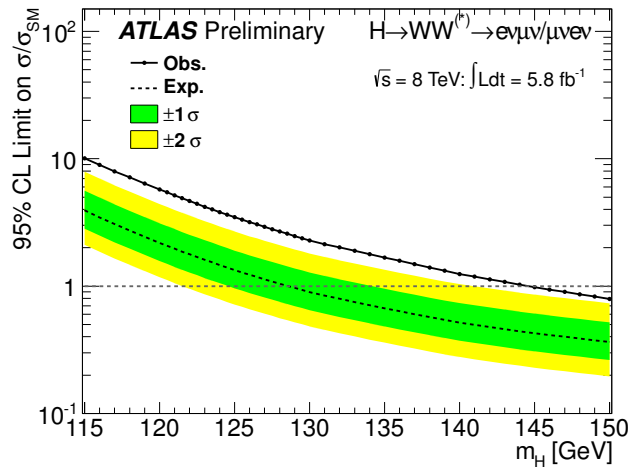
Figure 20: Observed (solid) and expected (dashed) 95% CL upper limits on the cross section, normalised to the SM Higgs boson production cross section and as a function of m_H, over the full mass range considered in the 8 TeV data. The green and yellow regions indicate the $\pm 1\sigma$ and $\pm 2\sigma$ uncertainty bands on the expected limit, respectively. Due to the excess of events observed in the low mass signal region, the corresponding mass points cannot be excluded as expected. The results at neighbouring mass points are highly correlated due to the limited mass resolution in this final state.
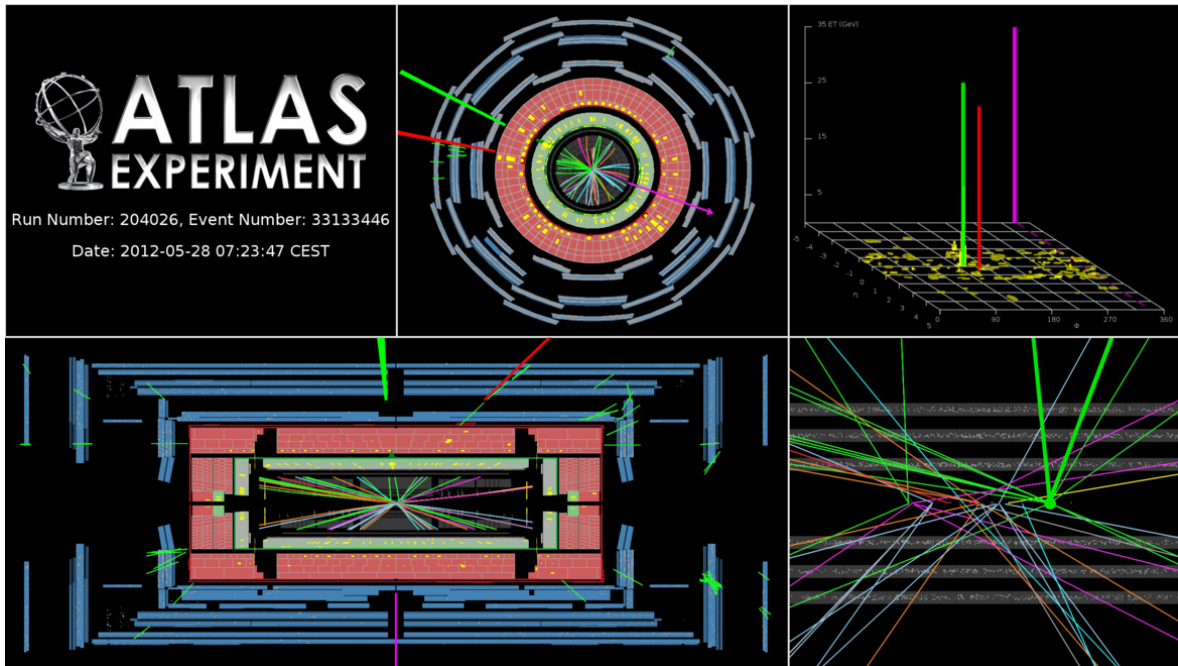

Figure 21: Display of an event satisfying all the selection criteria for events in the $H+0$-jet $e\mu$ channel. The reconstructed lepton p_T values are 33 and 29 GeV for the electron and the muon respectively. The reconstructed $E_{T,rel}^{miss}$ is 35 GeV and the m_T is 94 GeV.